2013

Modeling Tools for Conformal Orthotic Devices

Steven David Riddle
Purdue University, stevendriddle@gmail.com

Graduate School ETD Form 9
(Revised 12/07)

PURDUE UNIVERSITY
GRADUATE SCHOOL
Thesis/Dissertation Acceptance

This is to certify that the thesis/dissertation prepared

By Steven Riddle

Entitled
Modeling Tools for Conformal Orthotic Devices

For the degree of Master of Science in Mechanical Engineering

Is approved by the final examining committee:

Dr. Justin Seipel
Chair

Dr. Xinyan Deng

Dr. Jeffrey Rhoads

To the best of my knowledge and as understood by the student in the *Research Integrity and Copyright Disclaimer (Graduate School Form 20)*, this thesis/dissertation adheres to the provisions of Purdue University's "Policy on Integrity in Research" and the use of copyrighted material.

Approved by Major Professor(s): Dr. Justin Seipel

Approved by: David C. Anderson 04/19/2013
Head of the Graduate Program Date

MODELING TOOLS FOR CONFORMAL ORTHOTIC DEVICES

A Thesis

Submitted to the Faculty

of

Purdue University

by

Steven Riddle

In Partial Fulfillment of the

Requirements for the Degree

of

Master of Science in Mechanical Engineering

May 2013

Purdue University

West Lafayette, Indiana

ACKNOWLEDGMENTS

This thesis has been made possible by the intellectual contributions and support of many people, and I am thankful to all of them.

First, I would like to thank Arun Cherian for his collaboration developing the skin strain mapping technique and joint parameter experiment presented in this thesis. I am grateful to Arun for his leadership, guidance, and advice, both as a colleague in the field of conformal orthotics and as a friend. It has been my pleasure to work with such a talented and passionate individual.

Secondly, I am grateful to Dr. Justin Seipel for his passion toward scientific learning and his guidance shaping my academic pursuits and this thesis. The opportunities presented, challenges overcome, and conversations had over the last two years have helped me grow as a researcher and a person for which I am grateful.

Thirdly, I am grateful to all the individuals who have contributed to the experiments and analysis of the work in this thesis. For going above and beyond in assisting with data capture and analysis, often on short notice and for extended periods of time, I thank Will Hoggatt. For assisting with data capture and experimental setups and locomotion modeling, I thank Manish Anand. For their assistance with joint model fitting, I thank Dr. Jeffrey Rhoads and Jeffrey Ackerman. For his continued pursuit of locomotion friction experiments and comic relief, I thank Abhinav Kris Bhasin. For their assistance in ways both large and small, I thank the entirety of the Spira Lab group; you have made many things possible and kept life interesting.

Finally, I would like to thank my friends and family, near and far, for their support throughout the past two years. I am grateful to everyone at Purdue for their fellowship and supply of enjoyable excuses to leave the lab regularly. I've had the pleasure of great conversation and more new adventures than I can easily recall; the last two years have been a great experience and you are directly responsible.

As for my family, I would like to thank you for your love, support, excuses to get away, concern, and encouragement over not only the last two years but my entire academic career. You've helped keep me sane and moving forward by reminding me what is truly important in life. I am extremely blessed and grateful for all of you.

TABLE OF CONTENTS

LIST OF TABLES

LIST OF FIGURES

Figure Page

SYMBOLS

b	Damping
g	Gravity
I	Inertia
I_p	Inertia about Proximal Side of the Leg
k	Linear Stiffness
k_q	Quadratic Stiffness
k_c	Cubic Stiffness
L	Leg Length
L_p	Proximal Leg Length to CoM
M	Body Mass
m	Leg Mass
v	Velocity
α_{RFF}	RFF Tuning Constant
ρ_p	Radius of Gyration from Proximal Side of Leg
σ	Standard Deviation
ζ_o	Unstretched Leg Length, CT-SLIP

ABBREVIATIONS

AFO	Ankle-Foot Orthosis
CoM	Center of Mass
CT-SLIP	Clock Torqued Spring-Loaded Inverted Pendulum
DOF	Degree of Freedom
EOM	Equations of Motion
GC	Gait Cycle
LO	Liftoff Event
LoNE	Lines of Non-Extension
RFF	Relative Force Friction
RHex	Rotary Hexapod
SLIP	Spring-Loaded Inverted Pendulum
TD	Touchdown Event

ABSTRACT

Riddle, Steven MSME, Purdue University, May 2013. Modeling Tools for Conformal Orthotic Devices. Major Professor: Justin Seipel, School of Mechanical Engineering.

The purpose of this thesis is to advance the design of conformal orthotic devices through the development of two modeling tools to address knowledge gaps in the field.

The field of human orthotics has been continually troubled by identifying successful methods of harnessing devices to the body. Past orthotics have utilized a rigid framework with minimal degrees of freedom (DOFs) driven by hard actuators attached to the body at select anchor points. Many devices design the structure and anchor points such that they reduce the degrees of freedom of a targeted joint, limiting the user's mobility and often causing the structure to slide relative to the body as much as actuate a given joint.

There has been a recent shift in the orthotic field toward biologically inspired conformal structures to address the limitations of hard systems. By focusing on conformal devices that move with the body, limited DOFs and mobility restrictions can be addressed while also enabling new possibilities in human augmentation devices. Conformal orthotics have the opportunity to allow more DOFs in a joint while performing the same task as their rigid counterparts. By allowing these additional DOFs, the overall mobility of the user could be increased and more nuanced and particular interactions with the body and the environment may be possible. More channels of actuation could lead to finer joint control and enable more complicated tasks to be performed.

The task of designing conformal orthotic structures can be broken into four parts: developing 3D skin strain models; identifying minimum strain contours for orthotic

structures; modeling the effect of these structures on a joint's motion; and modeling how the modified joint behaves during a human task, such as locomotion. Much work has been done in each of these design fields; however, there remain several knowledge gaps in the field preventing the realization of conformal orthotics that need to be addressed.

Addressing the first gap requires the creation of minimum strain contours on the skin surface using the 3D skin strain field as reference. Addressing the second gap requires modeling how conformal orthotic structures based on minimum skin strain contours affect joint parameters. Addressing the third and final gap requires modeling the effect of modified joint parameters on a given task. There is a need to improve understanding of these knowledge gaps so that conformal orthotics can be appropriately designed and implemented for a given task.

To address the first and second conformal orthotic knowledge gaps, this thesis presents a modeling tool for mapping 3D skin strain on the skin surface and analyzing the effect of conformal orthotic structures on joint parameters. Joint parameters are compared to a control and conformal structures are found to have minimal impact on passive joint parameters.

To address the third conformal orthotic knowledge gap, a locomotion model with frictional effects is developed to improve quantitative prediction capabilities, and the effect of friction is experimentally verified. Friction was found to have a significant effect on the dynamics of legged locomotion models.

1. INTRODUCTION

Orthotic devices to modify human motion have been in existence for over a century; from simple braces to treat joint related injuries commonly seen in athletics to complicated structures designed to influence structural development [1]. In the past decades, the field of human augmentation devices, commonly referred to as exoskeletons, has been expanding rapidly with great developments related to enhancing human motion [2]. In recent years, there has been a design shift away from using rigid structures and actuators in these devices to using conformal structures [3,4] and compliant actuators [5]; the emerging field of conformal orthotics. However, despite the significant advancement of conformal orthotic designs in the last few years, there remain several knowledge gaps in the field preventing the realization of conformal orthotics that need to be addressed.

1.1 Motivation

A fundamental issue in orthotic design is that joint motion must be augmented to correct a pathological defect or enhance motion while not unnecessarily encumbering or restricting the user. To achieve this, past orthotics have utilized a rigid framework with minimal degrees of freedom (DOFs) driven by hard actuators attached to the body at select anchor points [2]. As the body moves through its daily routine of dynamic motion, the actuators or restraining structures inject energy in targeted DOFs. This injection of energy results in augmented joint motion. This augmentation of joint motion is not always efficient, often causing the structure to slide relative to the body as much as actuate a given joint and thereby reducing or neutralizing the device's intended effect. To address this relative motion, many devices' structures

and anchor points are designed such that they reduce the DOFs of a targeted joint, further limiting the user's mobility and increasing metabolic cost of transport [6].

There has been a recent shift in the orthotic field toward biologically inspired actuators and structures to address the limitations of hard, rigid systems. The advent of adaptable, passive-compliant actuators such as series elastic actuators has enabled safer human device interactions [7,8]. By interfacing with a human through a compliant mechanism, large impulse loads on the body can be reduced and a safety barrier to prevent damaging actuation established [5, 7].

In addition to biologically inspired actuators, there has been significant study into conformal structures that are worn close to, and move with the body. Initially focused on the design of high mobility spacesuits [9, 4], the analysis of skin strain during human locomotion enables the design of optimal structures for conformal orthotic device harnessing [10]. By focusing on conformal devices that move with the body, limited DOFs and mobility restrictions can be addressed while also enabling new possibilities in human augmentation devices. Without rigid joint structures, conformal orthotics could allow more DOFs in a joint while performing the same task as their rigid counterparts. By allowing these additional DOFs, the overall mobility of the user could be increased and the cost of transport reduced [6]. With additional DOFs in joints, more nuanced and particular interactions between the body and the environment may be possible. More channels of actuation could lead to finer joint control and enable more complicated tasks to be performed, such as navigating rocky terrain and dancing. While the breadth of possibilities for conformal orthotic devices is unknown, the potential gains make them worth pursuing.

The task of designing conformal orthotic structures can be broken into four parts, as seen in Figure 1.1. Part 1 comprises developing a 3D skin strain model of the appendage to be augmented. Much work has been done in the past few years to characterize human skin strain [3, 10, 11]. Part 2 comprises analyzing the skin strain field to identify minimum strain contours for conformal orthotic structures. While this part has been addressed [10, 11], there remains much room for further study of

identifying optimal strain contours. Part 3 comprises developing models of how these conformal orthotic structures affect joint parameters. There are models in physiology for studying joint motion [12], but they have yet to be utilized in orthotic design. Part 4 comprises modeling a given human task, such as locomotion, lifting, or climbing, so the effect of these modified joint parameters can be studied. Many locomotion models have been developed to study legged locomotion [13, 14]; however, apart from overall trend matching of trajectories and forces at steady state [13], little has been done to develop locomotion models with quantitatively accurate predictions.

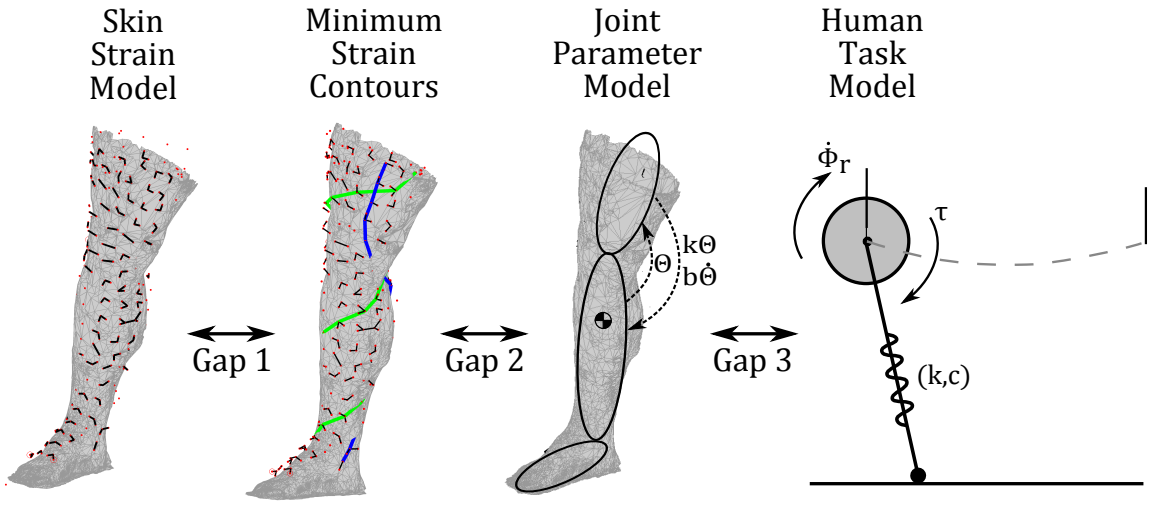

Figure 1.1. The emerging field of conformal orthotic design faces many knowledge gaps preventing their implementation. Gap 1 comprises mapping skin strain fields to minimum strain contours. Gap 2 comprises modeling how these minimum strain contours affect joint motion. Gap 3 comprises modeling how these modified joint parameters affect a joint task, such as locomotion.

There are three knowledge gaps, shown in Figure 1.1, that must be addressed for the practical implementation of conformal orthotic devices. Addressing gap 1 requires the creation of minimum strain contours on the skin surface using the 3D skin strain field as reference. The current best practice involves the use of hand interpolation to connect strain nodes [3, 10]. Though automated approaches have been suggested,

none have been developed [11]. Addressing gap 2 requires modeling the effect of conformal orthotic structures based on minimum strain contours on joint parameters. The hypothesis of the field is that an ideal structure can be designed that applies no external resistance to the joint, or requires no work to move [9]. While qualitative assessments of joint performance with these structures has shown encouraging results, they have not been quantitatively studied [15,3]. Addressing gap 3 requires modeling the effect of modified joint parameters on a given task. Many simplified task models have been developed for studying human locomotion [16]; however, while they have qualitatively accurate results, they lack quantitatively valid predictions of locomotion behavior [14]. There is a need to bridge these knowledge gaps so that conformal orthotics can be appropriately designed and implemented for a given task.

To address the first and second conformal orthotic knowledge gaps, this thesis presents a modeling tool for mapping 3D skin strain on the skin surface and analyzing the effect of conformal orthotic structures on joint parameters.

To address the third conformal orthotic knowledge gap, a locomotion model with frictional effects is developed to improve quantitative prediction capabilities, and the effect of friction is experimentally verified.

1.2 Problem Statement

The purpose of this thesis is to advance the design of conformal orthotic devices through the development of modeling tools to address knowledge gaps in the field. The specific research objectives of this thesis are as follows:

1. *Develop a technique to model the effect of conformal knee orthotic structures on passive knee joint parameters.*
2. *Develop an improved locomotion task model through the addition of frictional effects to improve the quantitative accuracy of the center of mass motion and experimental verify results.*

1.3 Hypotheses

1. *Conformal orthotic structures placed along the minimum strain contours will have negligible effect on passive knee joint parameters while remaining conformal to the skin.*
2. *The addition of frictional effects to a locomotion task model will improve the quantitative prediction power of the model without a significant increase in complexity.*

1.4 Roadmap to Thesis

This thesis offers the reader background information on the topic of non-conformal and conformal orthotic devices, explains the development and analysis of two modeling tools for use in lower extremity exoskeleton development, and discusses the implications and limitations of these tools.

Chapter 2, Background and Literature Review, begins with a discussion of lower extremity anatomy and an overview of the current challenges and state-of-the-art in lower extremity exoskeletons and orthotics. Next, the bio-mechanical structure of human skin is introduced and previous literature on skin strain theory and experimentation is reviewed. The chapter continues with the topics of *in vivo* measurement of human skin strain and evaluation of passive joint parameters with an introduction to the Wartenberg pendulum test. The chapter concludes with an introduction to the basic mechanics of locomotion and previous efforts to develop predictive models.

Chapter 3, Mapping the Minimal Skin Strain Vector Field of the Human Body, introduces an improved technique for mapping the lines of minimal skin strain along the human body, simplifying the process, and digitizing the data. The technique directly identifies the strain field on a subject, enabling immediate verification testing of various orthotic concepts based on minimum skin strain. This technique enables the development of passive joint parameter models in Chapter 4.

Chapter 4, Verifying the Minimal Skin Strain Vector Field Based Orthotic Wraps, explores the various possible orthotic wraps that can be aligned to the skin strain

vectors and provides a modeling tool to study the effect of conformal orthotic structures on the passive joint parameters of the knee. These joint parameters can then be used for predicting how conformal orthotic structures will affect a human task, such as locomotion.

Chapter 5, Locomotion Task Model, expands an established template model for biped locomotion through the addition of friction and studies the effect of changing friction on the model's motion. An experimental study of changing contact friction parameters on bipedal legged locomotion is conducted. Improved, quantitatively accurate locomotion models can be used with the joint parameter models to study the effect of conformal orthotic structures on human locomotion.

Chapter 6, Conclusions, contains reflections on the skin mapping technique developed, and on its use for testing minimum skin strain contours on the lower extremities. Limitations of the mapping method and joint parameter modeling of the leg are discussed, and recommendations for future work given. Furthermore, this chapter considers the implications of friction on locomotion models and robotic platforms and addresses the limitations of the efforts presented herein. Finally, the thesis ends by restating the key contributions made in this work.

2. BACKGROUND AND LITERATURE REVIEW

Before discussing the lower extremity skin strain mapping and contour analysis that is the main objective of this modeling tool, an overview of the background information, previous research, and relevant physical concepts is necessary. This chapter begins with a discussion of the basic physics of locomotion and an overview of the current challenges and state-of-the-art in lower extremity exoskeletons and orthotics. Next, the bio-mechanical structure of human skin is introduced and previous literature on skin strain theory and experimentation is reviewed. The chapter concludes with the topics of *in vivo* measurement of human skin strain, with an introduction to the use of motion capture systems, and on the evaluation of passive joint parameters, with an introduction to the Wartenberg pendulum test.

2.1 Lower Extremity Anatomy

An understanding the biomechanics of human walking is integral to the design of lower extremity orthotic devices. Therefore, a brief overview of human lower extremity anatomy is presented.

Locations on the body are described using the anatomical reference planes as seen in Figure 2.1(a). The relative positions of the body segments are described using the following anatomic directional terms from [17]:

Anterior Near to or at the front of the body.

Posterior Near to or at the back of the body.

Medial Nearer to the midline or sagittal plane.

Lateral Farther from the midline or sagittal plane.

Proximal Nearer to the attachment of a limb to the trunk, near to the origin.

Distal Farther from the attachment of a limb to the trunk, farther from the origin.

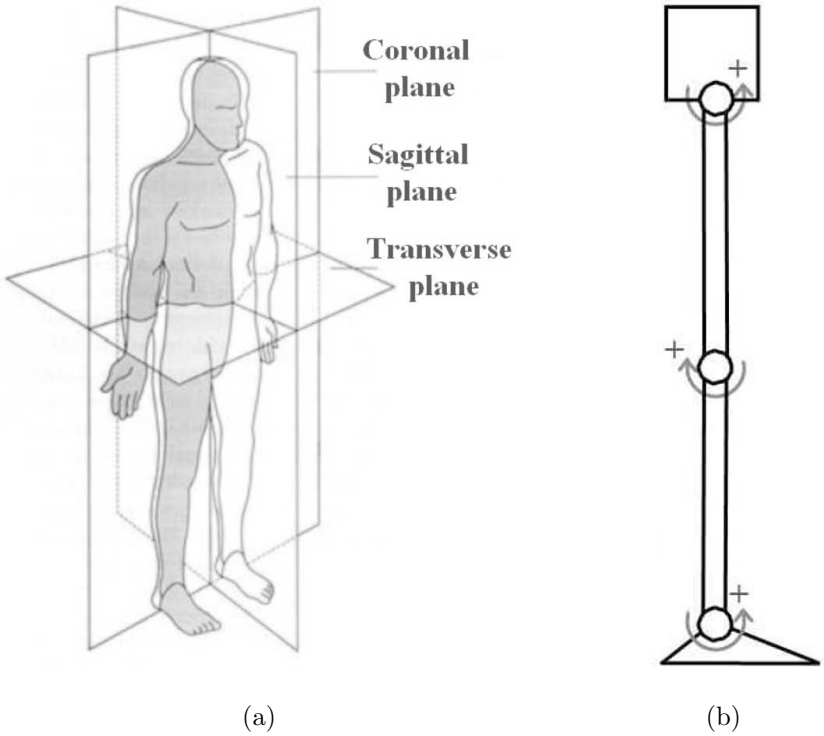

Figure 2.1. (A) Anatomical reference planes of the human body and (b) diagram of the leg at rest with positive joint motion indicated. Adapted from [2].

This thesis focuses on the lower limbs that are divided into three primary anatomic segments: thigh (portion from the hip to the knee), leg (portion from the knee to the ankle), and foot. In general, the leg can be considered as a 7 DOFs structure, with three rotational DOFs at the hip, one at the knee, and three at the ankle. During human locomotion, the lower extremity moves slightly in all the DOFs; however, the primary motions occur in the sagittal plane. In this thesis, the joint rotations of the lower extremity are described as follows (directional references seen in Figure 2.1(b)):

Hip Flexion Positive motion of hip.

Hip Extension Negative motion of hip.

Hip Abduction Motion of the hip in the coronal plane away from the center of body.

Hip Adduction Motion of the hip in the coronal plane towards the center of body.

Knee Flexion Positive motion of knee.

Knee Extension Negative motion of knee.

Ankle Dorsi-Flexion Positive motion of ankle.

Ankle Plantar-Flexion Negative motion of ankle.

Ankle Eversion Motion of the ankle in the coronal plane away from the center of body.

Ankle Inversion Motion of the ankle in the coronal plane towards the center of body.

Remaining DOFs of the hip and ankle have minimal motion during locomotion and are referred to simply as "rotation."

2.2 Orthoses and Exoskeletons

Other then mention in early patents and science fiction [18], research in powered human exoskeleton devices began in the late 1960s [2]. From the beginning, there were two distinct motivations for developing these powered devices: to augment the abilities of able-bodied humans, typically for military purposes, and to develop assistive devices for physically challenged persons. To date, both motivations have been actively researched, with breakthroughs in technology often helping both groups due to their similar set of challenges and constraints [2]. This section provides a brief overview of current exoskeletons and orthoses, for an in-depth history and review see [2].

Following common practice [2,19], for the purpose of this section an exoskeleton is defined as an active mechanical device that is essentially anthropomorphic in nature,

worn by the user, and works in sync with the operator. In short, "exoskeleton" is used to describe a device that augments the performance of an able-bodied user. Conversely, the term orthosis is typically used to describe a device that is used to improve the motion of a physically challenged user, either passively or actively. In practice, the terms "orthosis" and "exoskeleton" can be, and frequently are, used interchangeably [2, 20, 19, 1, 5].

2.2.1 Performance-Augmenting Exoskeletons

Following the convention established above, this section works to describe recent powered mechanical devices intended to augment able-bodied individuals. Within that definition, the majority of exoskeletons can be categorized as either designed for military purposes or for non-military uses.

Military Designs

The U.S. Defense Advance Research Projects Agency (DARPA) has been a major sponsor of exoskeleton research with the Exoskeletons for Human Performance Augmentation (EHPA) and subsequent programs. The goal of the program is to "increase the capabilities of ground soldiers beyond that of a human" [21]. The specific focus of the program was to augment the load-carrying capabilities of soldiers, improving endurance and reducing fatigue. Three institutions demonstrated working exoskeletons for the program: Berkeley Exoskeleton (BLEEX) [22], Raytheon Sarcos Exoskeleton [23], and the MIT Exoskeleton [24].

BLEEX is one of the first, and best known, energetically autonomous exoskeletons, carrying its own power source. Its developers claim it as the first "load-bearing and energetically autonomous" exoskeleton [22]. It features a total of 7 DOFs, 3 DOFs at the hip, 1 at the knee, and 3 at the ankle; 4 of the DOFs are actuated. The exoskeleton is actuated by linear hydraulic cylinders and users wearing the system can reportedly support a load of $75kg$ while walking at $0.9\frac{m}{s}$ [25]. The current generation of BLEEX,

known as the Human Universal Load Carrier (HULK), is under joint development by Berkeley Bionics and Lockheed Martin [26].

Raytheon Sarcos has developed a full-body "Wearable Energetically Autonomous Robot (WEAR)" also under the DARPA EHPA program. The Sarcos exoskeleton uses rotary hydraulic actuators to directly power the joints. The Sarcos exoskeleton has reportedly demonstrated entirely supporting a $84kg$ load and walking at $1.6\frac{m}{s}$ while carrying $68kg$ on the back and $23kg$ on the arms [23]. The program has been transitioned to the Army for further development.

The MIT Exoskeleton is unique in the group as a quasi-passive exoskeleton design by the Biomechatronics Group at Massachusetts Institute of Technology Media Laboratory. The MIT exoskeleton employs a quasi-passive design that does not use any actuators for adding power at the joints. Instead, the design relies completely on the controlled release of energy stored in springs during the (negative power) phases of the walking gait [24, 27]. Due to the conservative actuation strategy, the MIT Exoskeleton requires minimal power ($2W$). In addition, significant work was done to evaluate the metabolic cost of using the exoskeleton. Studies showed a metabolic increase of 10% when carrying a $36kg$ load. Further study concluded that a dominant cause for the observed cost of transport increase was the additional kinematic constraints imposed on the wearer [28].

Commercial Designs

In addition to the exoskeletons designed for military purposes, there is also growing research into devices targeted for commercial use. A notable example is the Hybrid Assistive Leg (HAL) developed at the University of Tsukuba, Japan. The exoskeleton is targeted for both performance-augmenting and rehabilitative purposes [29,30]. The full-body (HAL)-5 exoskeleton powers the hip and knee joints using a dc motor with harmonic drive to directly drive the joints while the ankle joint is passive. The system

is capable of enabling a user to carry up to $40kg$ on their arms. The system is currently being commercialized by Cyberdyne (Tsukuba, Japan).

2.2.2 Active Orthoses

Following the convention established above, this section works to describe recent powered mechanical devices intended to augment physically-challenged individuals. These devices typically aim to improve on passive orthoses designs through the addition of power. Within that definition, the orthoses can be generally categorized the joint they are designed to effect, with ankle-foot orthoses (AFO) being the most common device.

Ankle-Foot Orthoses (AFO) are typically developed to provide an assist in flexion/extension of the ankle. This is commonly achieved at the expense of the remaining ankle DOFs, effectively creating a 1 DOF joint.

The MIT Biomechatronics Group developed a powered AFO to assist dropfoot gait, a common affliction for in stroke patients [31]. The device consists of a modified passive AFO with the addition of a series-elastic actuator to allow for the variation in impedance of ankle flexion/extension. The device was successful in clinical trials, increasing walking speed and reducing the instances of "foot slap." Efforts to make the device more portable are underway.

The Human Neuromechanics Laboratory at University of Michigan has developed a number of powered AFOs designed for in-clinic rehabilitation of patients. These devices are typically tethered and unable to leave the lab setting. The devices use artificial pneumatic muscles and carbon fiber frames along with custom fit polypropylene shells to reduce weight and improve fit. The Human Neuromechanics Laboratory has built AFOs with agonist/antagonist pairs, as well as, a single plantar flexion actuator [32].

Arizona State University has developed an AFO using a series elastic actuator design, called a robotic tendon [20], to supplement flexion/extension of the ankle

throughout gait. The device takes advantage of a tuned spring to store and release energy during the GC, minimizing the active power requirements of the device. The robotic tendon technology has also been successfully worked into a prosthesis [33].

2.3 Biomechanical Properties of Human Skin

While research on the design of exoskeletons and orthoses has been steadily making progress with injecting power into the gait cycle to improve locomotion, there has been little research into the comfort and fit of these same devices. Looking at the device/body interface, the skin, can lead to new ways to interface orthotic devices. Study of the human body reveals that the skin behaves much as an elastic surface. By investigating the movement patterns of the skin through normal joint movements, it can be observed that the skin stretches more in some directions than others; suggesting an elastic strain field. If an orthotic device's structure could be aligned with the directions of minimum skin strain, it may reduce movement relative to the skin. If a structure could lie along lines of minimum skin strain, it may be possible to attach a structure to the human body and have it move naturally with the joints without resisting motion. This desire leads to a further investigation of the device/body interface, the skin.

2.3.1 Structure of Human Skin

The structure of the skin can be divided into two heterogeneous main layers, the epidermis and the dermis (Figure 2.2) [34, 35]. The skin layers are very distinct in their nature, structure, and properties [36].

Epidermis, the thinner superficial layer of the skin with between $0.06mm$ and $1.00mm$ thickness, is composed of keratinized stratified squamous epithelium [34,37]. About 90% of epidermal cells are keratinocytes which produce keratin. Keratin is a tough fibrous protein that protects the skin and the underlying tissues. About 8% of the epidermal cells, called melanocytes, are responsible for producing the melanin

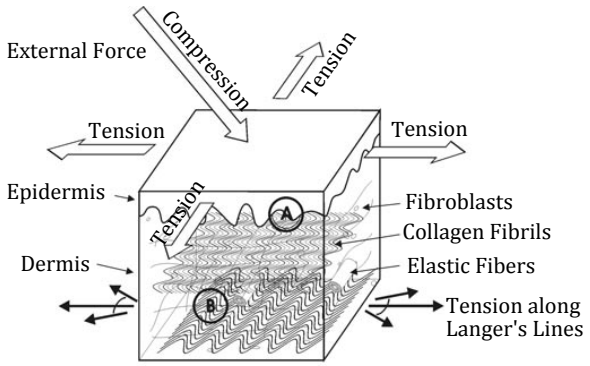

Figure 2.2. Structure of skin and external and internal force transmission. Reproduced from [34].

pigment. The Langerbans cells and Merkel cells are the remaining cells of the four main types present in epidermis. Langerbans cells participate in skin immune response and Merkel cells are associated with the sense of touch discrimination of shapes and textures [37, 10].

Dermis, the deepest layer of the skin, with a thickness of $1 - 4mm$, is mainly composed for connective tissue containing collagen and elastic fibers [37]. This layer is divided into three sub layers: papillary, sub-papillary and reticular layer [38]. The superficial part of the dermis is composed of connective tissue containing thin collagen and rich elastic fibers. Its surface area is increased by small projections, called dermal papillae, that retain significant amounts of water [38]. The deepest part of the dermis is composed by a dense irregular connective tissue that contains bundles of collagen and some coarse elastic fibers. Adipose cells, hair follicles, nerves, oil glands and sweat glands are between these fibers. The collagen and the elastic fibers present in the reticular region give strength, extensibility (ability to stretch) and elasticity (ability to return to the original shape after stretching) to the skin [39, 37, 38, 40, 10].

2.3.2 Properties of Human Skin

The mechanical behavior of the different components of skin and how they influence the mechanical properties of each layer are fundamental in understanding the complex mechanical properties of the human skin. *In vivo* human skin is mechanically heterogeneous (i.e., properties vary on the anatomic region), anisotropic (i.e., mechanical properties depend on the direction), viscoelastic (i.e., skin stress is a function of time and strain), non-linear and under tension and its properties are affected by many factors such as age, gender, race, anatomic region, physiological conditions, hormonal status, skin disorders and the use of different skin care products [36, 41, 3, 35]. Furthermore, the mechanical behavior of the superficial layer of the epidermis, the stratum corneum, is strongly influenced by the environmental conditions, such as temperature and humidity [35]. Silver, et al. provides a thorough review of the mechanobiology of skin [34], and his remarks are summarized here with additional insights from [10].

The main component of the dermis layer are collagen fibers at about 77% of the fat-free dry weight. These fibers form an irregular network of wavy coils oriented almost parallel with the skin surface. These coils have a high stiffness and a low extensibility. Elastin fibers are the second main component of the dermis at about 4% of the fat-free dry weight. Elastin fibers are less stiff than the collagen and show reversible strains of more than 100% [35, 40]. Reticular fibers represent 0.4% of the fat-free dry weight and its mechanical properties are not exactly known [35]. The extracellular matrix, or ground substance, is responsible for the viscoelastic behavior of the dermis and does not contribute to the tensile strength of the dermis [35].

One of the major functions of the skin is the protection against external mechanical aggressions through the reversible deformation of its structure [40, 42]. Many non-invasive techniques have been developed to measure the properties of the human skin. The most used techniques are suction [39], torsion, traction, extensometry, and elastic wave propagation [42].

The main studies about the skins mechanical properties are focused on the mechanical behavior of the deepest layer, the collagen-rich dermis [35]. These studies show that the mechanical properties of the skin depend mainly of dermal and hypodermal collagen and the network of elastic fibers present in these layers [39]. However, the results of all studies performed *in vivo* are affected by the mechanical behavior of the epidermis since it is not possible to isolate the dermis or the hypodermis layers of the skin to test their properties without interference [35].

The skin is influenced by two types of forces: internal and external. The external forces are transmitted through the epidermis to the dermis and subcutaneous tissues and the internal forces are transmitted through the dermis to the epidermis [34].

The internal forces acting on the skin are due to both passive and active tension. The passive tension of the skin is caused by the collagen fibrils present in the dermis, these fibrils are approximately aligned along the Langers lines (section 2.3.3). The active tension is performed by the fibroblasts contraction of the collagen fibrils present in the extracellular matrix. These forces cause tension at the junctions between keratinocyte cells. The external forces further increase the keratinocyte-keratinocyte cell tension junctions also changing the dermis stress state [34].

The passive and active tensions are reflected on the skins mechanical behavior. The skin has an initial low modulus behavior which is due to the contribution of the elastic fibers to the recovery of the collagen networks on the skin. The collagen fibers have been modeled as a biaxial oriented network of wavy fibers that, in the presence of loads, align with the directions of these loads during deformation. The passive stress-strain behavior of the skin is composed of three phases (Figure 2.3, for uniaxial tension on the left and biaxial tension on the right). For the uniaxial tension, the first phase, for strains up to 30%, is characterized by a little resistance to deformation by the collagen network, and the elastic fibers define the skin behavior. In the second phase, for strains between 30% and 60%, the collagen fibrils offer some resistance to deformation and it is they who dominate the skin deformation in this linear portion

of the stress-strain curve. The third phase corresponds to the yield region, for strains above 60%, where fibrils defibrillation exists [34].

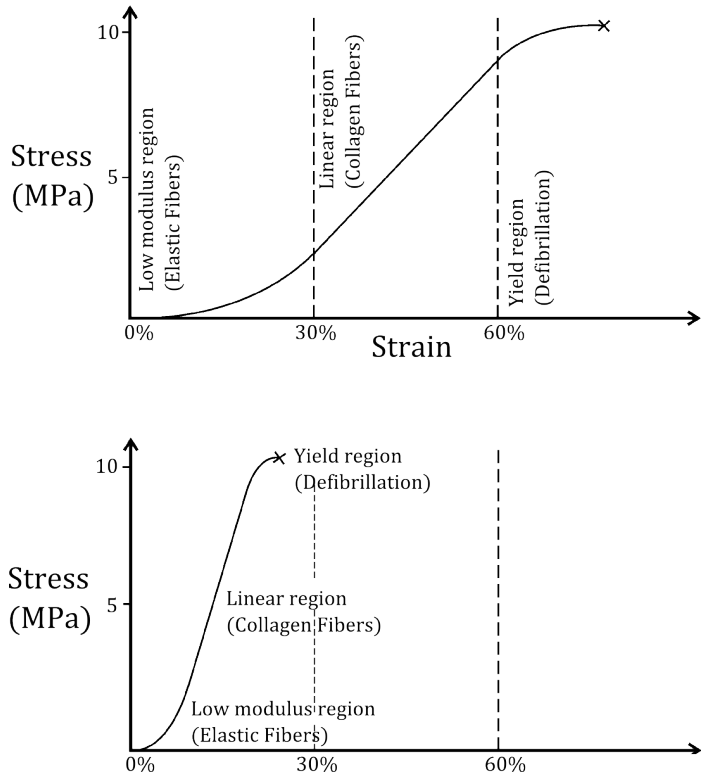

Figure 2.3. Generalized stress-strain curve of skin in uni-axial and bi-axial tension. Reproduced from [34].

Elastic stress-strain curves represent the stored energy by the collagen and elastic fibers stretching and the viscous stress-strain curves represent the energy lost due to the fibrillar slippage [34]. The viscoelastic properties and the stress relaxation behavior of the skin are dependent on the spatial orientation of the fibers [40].

Studies have shown that the skin does not usually operate in the low modulus region. The pre-stress is different for different body regions being greater in arms, sternum, thigh, patella and tibia and lowest in the back. Skin isotropy is highest in body regions where pre-stress have highest values. The bi-axial tension is the dominant load in human skin [43]. Biaxial skin in pre-stress is about 1MPa, which

results in 10% of the maximum strain, showing that, even in the absence of external loads, skin operates in the linear region of the stress-strain curve. The maximum stress in skin occurs after about 20% of biaxial strain and this value decreases with increased age [34].

The wall of the surface tissue breaks down when submitted to large mechanical loads. Therefore, the stress concentration in the interface skin/device leads to repeated tissue damage due to the mismatch between the mechanical properties of the skin and the device [43]. Initially, this stress causes a slight reddening on the surface that can develop into a significant injury that damages the tissues of the skin and can lead to chronic wounding [44,43]. One condition that leads to the development of skin injuries is the continuous use of orthoses [44]. Shear stress, even at low magnitudes, is a highly destructive loading modality, especially when applied over long time periods [43]. The relative motion of a device at its interface with the skin, during physical activity, fosters shearing that prevents the formation of an adequate skin seal [43]. Patients wearing orthoses are submitted to shear stress at the interface between the orthosis and the skin and this shear stress is one of the main causes of discomfort in the use of the existing orthoses.

2.3.3 Langer's Lines

The previous section describes the elastic behavior of the skin at a cellular level based on the interaction between the separate layers. The interaction between the collagen and elastic fibers results in a global understanding of the elastic nature of the skin. However, *in vivo* human skin is a mechanically heterogeneous (i.e., properties vary on the anatomic region) and anisotropic (i.e., mechanical properties depend on the direction) material [39]. This sparks interest in a local understanding of the elastic behavior of skin, specifically the strain magnitudes and directions.

The first research on the variability of skin stress and strain was conducted by Austrian anatomist Karl Langer in 1861. Langer observed that circular holes punched

in a cadaver's skin produced a "linear cleft" [45] instead of a round hole. This enlarged elliptical was caused by pre-stress along the across the major axes of the ellipse. Langer theorized that if the holes were placed close enough, they would map the lines of maximum pre-stress on the skin by connecting the long axes of all the ellipses [45]. Today, these lines are commonly referred to as Langer's Lines and can be seen in Figure 2.3.3.

Langers results showed that the lines tended to be parallel, however, they intersected at approximately right angles in some areas. According to Langer, the line directions in the areas of the face, back, and chest were the same for all individuals, while they tended to vary from individual to individual in the central forearm, lower leg and anterior abdominal wall. Langer believed these differences to be due to the different constitution of the cadavers [45].

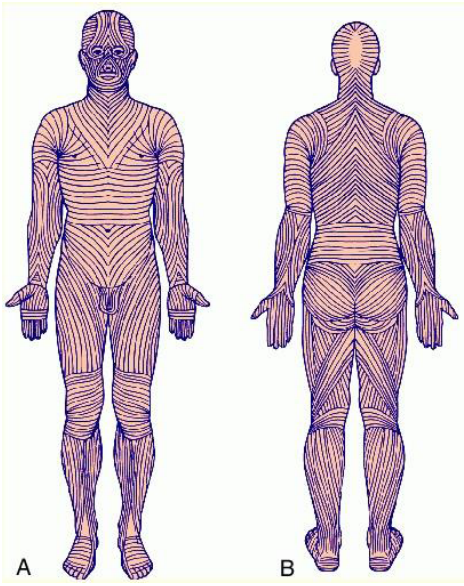

Figure 2.4. Representation of Langer's Lines in (a) anterior and (b) posterior views. Reproduced from [10].

In addition to the superficial observation of the direction of skin strain, Langer also studied the underlying structure of the skin. Upon examining an excised ellipse stretched along its major axis, Langer observed the underlying fibers to be tightly

grouped into a lattice of bundles. The major axis of the lattice had the same stretch direction as the excised ellipse, leading Langer to conclude the direction of the deformed ellipses was the same as the orientation of the skin fibers [45].

To this day, surgeons use Langer's Line as guidelines for orienting incisions during surgery. It is a commonly held believe among surgeons that orienting incisions as such results in narrower and less conspicuous scars [46]. However, other surgeon's argue that Langer's Lines vary too much from individual to individual to be of use in practice and are therefore more ritual than science [47].

2.3.4 Lines of Non-Extension (LoNE)

Lines of non-extension (LoNE) were originally theorized by A. Iberall in the 1950s for use in the design of a mechanical counter-pressure suit for experimental aircraft pilots, and eventually astronauts, for the United States Air Force. Iberall theorized building a pressure suit's structure along these LoNE would result a suit that required no additional work to move or orient a user's body when wearing the suit than when not wearing the suit. The design of this 'no-work' suit would be such that it applied no external torque to joints while moving and remains conformal to the body. In addition if the suit was designed well, it would not restrict or impede the user's range of motion [9].

Iberall suggested the body was covered in a grid of lines whose edges only experienced rotation, with no stretch, during human motion [9]. By observing the elastic deformation of circles drawn on the human skin, Iberall was able to identify these lines. Following with the theory of elasticity, the circles drawn on the skin deform into ellipses during human motion [9]. Iberall considered the assumption of small strains was satisfactory [15]. An example of the deformed circle can be seen in Figure 2.5. The intersection points between the original circle and deformed ellipse mark the directions of non-extension. Iberall developed a protocol for identifying minimum

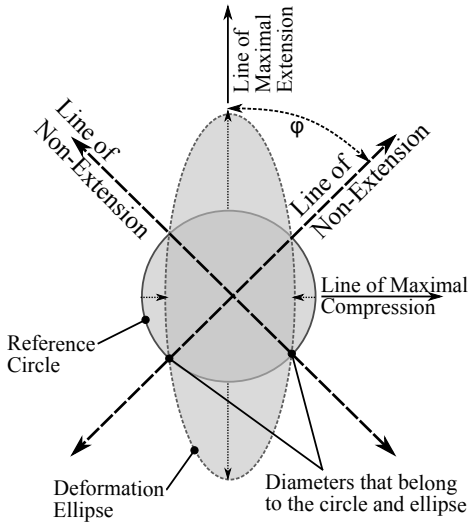

Figure 2.5. Iberall's strain ellipse method of identifying Lines of Non-Extension (LoNE) on human skin. The intersections of the reference circle and deformed ellipse define the LoNEs. Adapted from [3].

skin strain vectors along the body called 'lines of non-extension,' the results of which can be seen in Figure 2.6 [9, 15].

Following development of the LoNE seen in Figure 2.6, Iberall studied the consistency of the grid for difference deformations of the joints. He was able to verify that the line remain essentially consistent for all deformations, the practical benefit being that LoNE mapped at the extremes of joint deformation are valid for intermediate deformation [9].

Iberall's method relies on observation of the strain ellipses and as such is an approximation of minimal strain, with some human error induced. Iberall himself noted that the method had limitations, especially in areas of small deformation [9]. The large potential error induced by Iberall's method has lead many researchers to use numerical methods to identify skin strain in the human body [3, 10, 11].

In 2000, Dr. Newman at the MIT Man Vehicle Laboratory began investigating designs for high mobility space suits. She revitalized the concept of lines of non-extension set forth by Iberall for a new mechanical compression suit design, commonly

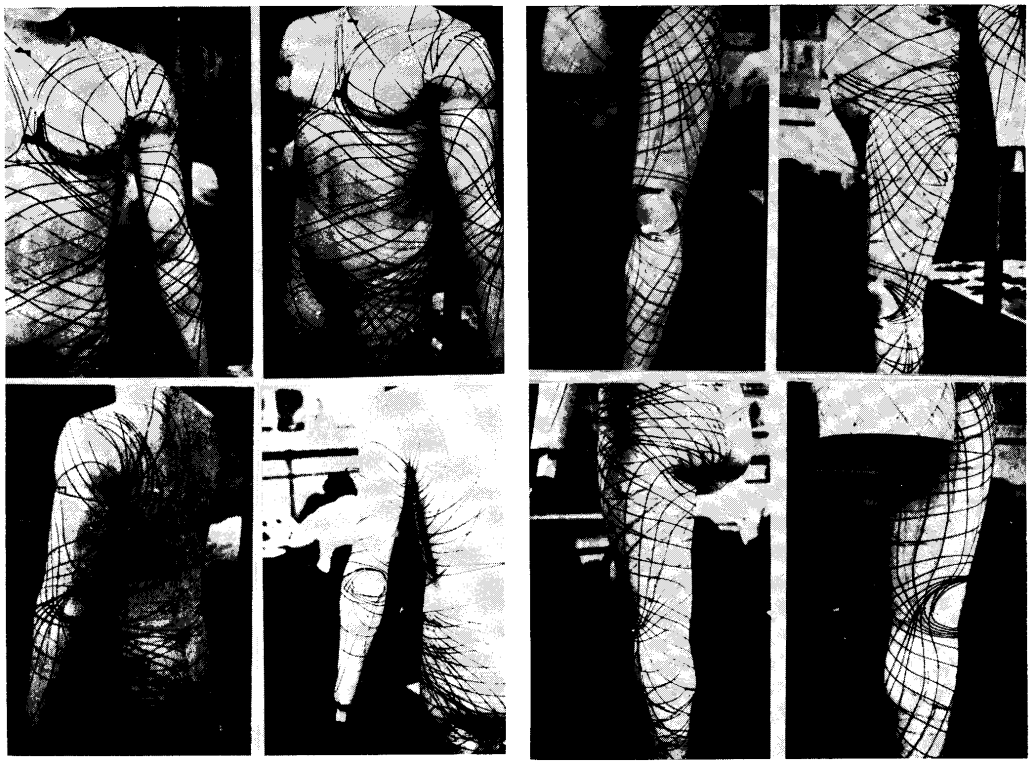

Figure 2.6. Depiction of Iberall's Lines of Non-Extension. Reproduced from [15].

known as the Bio-Suit [4]. An artist rendering of the Bio-Suit can be seen in Figure 2.7.

In 2005, K. Bethke, a graduate student under Dr. Newman, developed a repeatable and quantitative technique for determining and displaying the strain field on the skin surface of the human body in motion [3]. Unlike Iberall's study, this technique included the use of precision laser scanning for data collection, a computational algorithm for data analysis, and a visual display of the analysis's results. The strain field representation provided two types of strain information for a representative sample of body surface points: 1) the normal and shear strain in the body limb's local longitudinal and circumferential directions, and 2) the directions and magnitudes of minimum normal strain, or "minimum stretch." Figure 2.8 shows the directions of

Figure 2.7. Artist rendition of MIT Bio-Suit concept based on Iberall's LoNE. Reproduced from [4].

non-strain in the skin. The study observed only the right leg, using knee flexion as a representation of locomotion [3]. In additional to the numerical analysis of skin

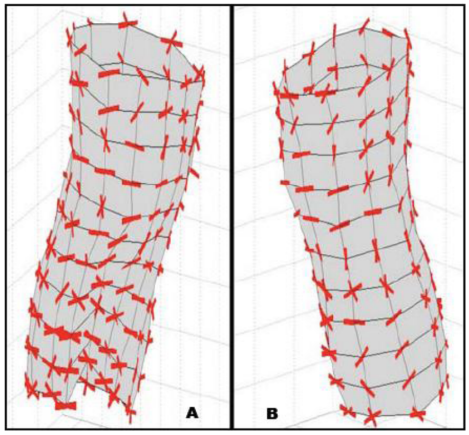

Figure 2.8. Directions of minimum normal strain during knee flexion, obtained by Bethke. (a) Anterior leg's view. (b) Posterior leg's view. Reproduced from [4].

strain on the subject's right knee, a prototype device was also built using the resulting minimal skin strain lines. The prototype consisted of inextensible wires wrapped in

intersecting lines on the subjects leg. The prototype was tested for knee flexion, seen in Figure 2.9, and the subject reported no movement restricts or discomfort. This test confirmed the existence of LoNE and the possibility of building rigid structures based on them without impairing movement.

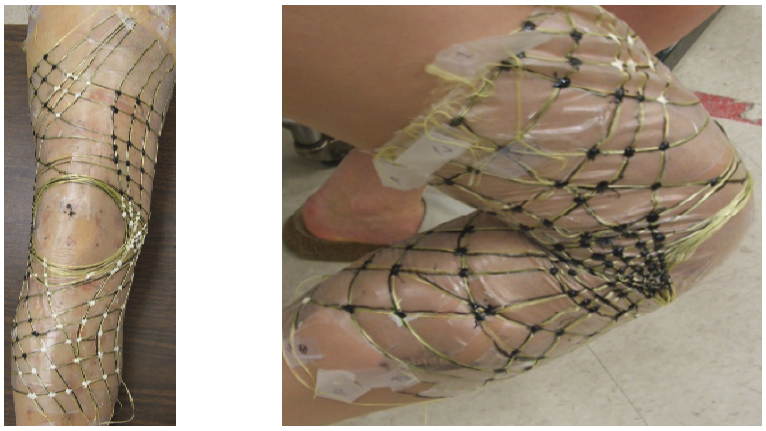

(a) (b)

Figure 2.9. MIT LoNE prototype developed by Bethke. (a) Knee in full extension. (b) Knee in full flexion. Reproduced from [3].

In 2010, S. Marreiros performed an in-depth analysis of the skin strain field of the human ankle joint, building on the previous protocol developed by Bethke. The study focused on strain maps of the ankle and foot's skin for the ankle's large movements and the directions of the LoNE in the same region [10]. An infrared motion capture system was used to capture the spatial position of reflective markers placed on the skin and a computational program was developed to calculate the principal skin strains. LoNE were found and drawn in the analyzed region of the foot, seen in Figure 2.10. Correlation was found between this study's LoNE map and previous results [15,3,10].

In 2012, A. Wessendorf, a graduate student under Dr. Newman, developed a new technique, improving on the methods of Bethke and Marreiros, to dynamically measure skin movement and strain around the knee during a squatting motion. With

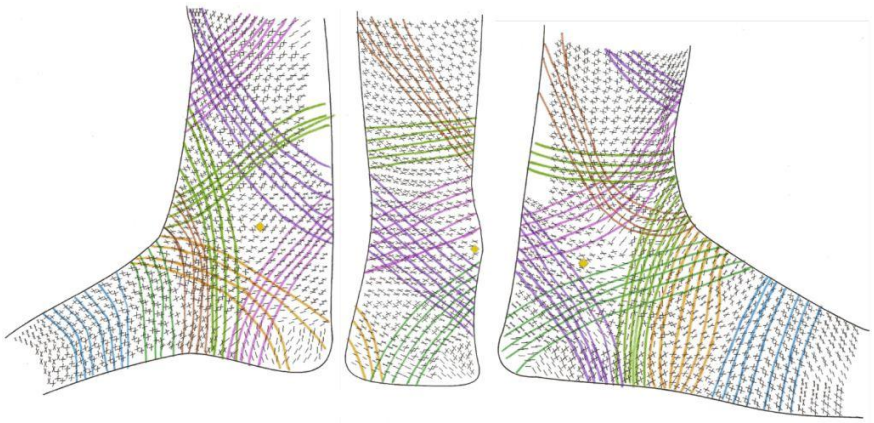

Figure 2.10. Marreiros's LoNE on the ankle for full extension/flexion. Reproduced from [10].

this new data, they were able to calculate the local direction of lines of non-extension, lines of minimum extension, and lines of minimum compression throughout the joint motion. An infrared motion capture system was use to acquire the position of markers on a subject's leg and then analyzed to determine skin strain and LoNE [11]. For a presentation of the data, refer to [11]. In general, the LoNE directions were found to align with previous analysis [15, 3, 11].

With the exception of Bethke [3], all of the recent research on LoNE have focused entirely on developing new techniques for characterizing the minimum strain field of a subject's body. Research has now established the existence of LoNE on the skin and developed sufficient methods for analyzing and digitally storing the strain field. [3, 10, 11]. Furthermore, a comparison of recent LoNE skin mapping efforts to Iberall's original work show that they are in agreement, validating the accuracy of Iberall's technique. A method of mapping skin strain based on Iberall's technique is developed with this assertion in mind in Chapter 3. The presented technique allows this thesis to push forward with developing methods to analyze the effectiveness of LoNE based structures for use in the design of exoskeletons and orthoses.

2.4 Evaluation of Passive Joint Parameters

Iberall originally envisioned the use of LoNE to create a 'no work' suit, that is a suit when worn by a user requires no additional work to move or orient their body than when not wearing the suit. In additional, if the suit is designed well, it would also not restrict or impede the user's range of motion. The design of this 'no-work' suit would be such that it applies no external torque to joints while moving and remains conformal to the body. [9]. It is from Iberall's definition of a 'no-work' suit that a method for evaluating conformal structures based on LoNE was developed.

2.4.1 Wartenberg's Pendulum Test

Evaluating the net effect a device causes on a joint's movement can be done by studying the effective change in passive joint parameters. The pendulum test of Wartenberg [12] is a technique commonly used to measure passive knee motion with the aim to assess spasticity. Skeletal muscle spasticity is described by physical therapists as increased resistance of a particular muscle group to manually induced passive movement [48]. When a joint with high spasticity is passively released from full extension, the extensor muscles involuntarily flex causing a resistive torque on the joint and reducing movement. The pendulum test measures the joint's movement to evaluate the level of involuntary muscle activation [12]. In addition to measures of spasticity, the pendulum test has also become a standard tool in kinesiology for the evaluation of joint stiffness and viscosity [49].

Wartenberg's Pendulum Test has found favor with many physicians due to its simplicity and lack of specialized equipment [50]. To conduct the test, the lower leg of a subject is extended over the ledge of a flat surface. The knee is brought to full extension and then released while the leg angle is measured. The test can be seen in Figure 2.11. The joint angle has historically been measured with an electro-goniometer [50], though the use of video to track the joints position has grown in popularity [51].

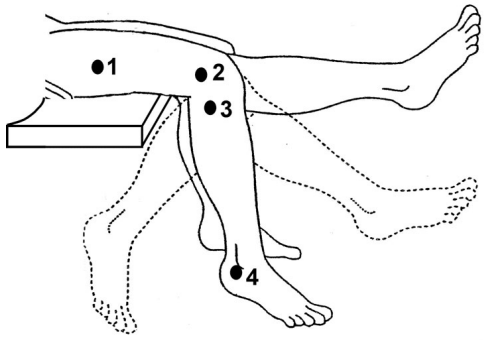

Figure 2.11. A demonstration of Wartenberg's Pendulum Test. The leg is suspended over a ledge and then allowed to fall in free response from full extension. Standard tracking marker locations for measuring knee angle are displayed. Reproduced from [49].

Using Wartenberg's Pendulum Test, the passive dynamics of the knee can be efficiently measured [49]. By performing a control test with no orthotic device, the base properties of a subjects need can be determined. By comparing the control test to an additional test with a LoNE structure, the effect of a LoNE structure on a joints passive dynamics can be determined. A study using Wartenberg's Pendulum Test is presented in Chapter 4 for structures based on LoNE.

2.5 Legged Locomotion Models

Biological walking is composed of a complicated set of actions, utilizing multiple muscle groups, embedded sensing and feedback, and complex control systems. Tens of degrees of freedom and hundreds of parameters characterize these systems, which have been fine-tuned through countless generations of organisms that need to move effectively and efficiently to survive and pass on their genes.

2.5.1 Walking Gait Cycle

Normal walking can be described as a series of equal gait cycles (GCs) or *strides* [19]. A simplified diagram of the human walking gait can be seen in Figure 2.12 (reproduced from [2]). Note that the timing of the label events during the GC are approximate and varies across individuals and conditions. The human walking GC is typically represented as starting (0%) at the point of heel strike and ending (100%) at the same heel striking again.

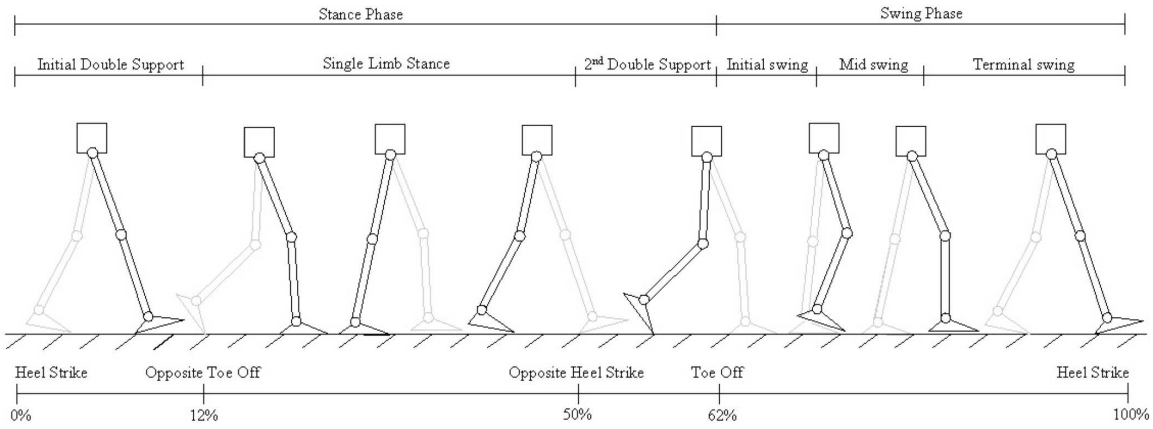

Figure 2.12. Human walking gait through one cycle, beginning and ending at heel strike. Percentages showing contact events are given at their approximate location in the cycle. Reproduced from [2].

The GC is composed of two main phases, stance and swing. The stance phase corresponds to when a foot is in contact with the ground, typically beginning at heel strike and ended at toe off. The swing phase corresponds to when a foot is in the air and pass by the opposing foot on the ground for forward advancement. During walking gaits, it is possible for both feet to be on the ground at the same time, which is known as double-stance. During faster gaits, it is also possible for both feet to lift off the ground at the same time, which is known as a flight phase. Flight phases are typically seen during running [19].

2.5.2 Templates and Anchors

Models of dynamic locomotion are greatly simplified and must operate with relatively few parameters to allow for analysis and understanding of the parameter space. Approaches to this task generally fall into one of two categories: templates or anchors. Templates are simple models that attempt to replicate the dynamics of a system through the use of familiar structures like springs and masses. Templates offer qualitative explanations for dynamic locomotion systems and allow for broad application to multiple organisms. Anchors are models that are more physiologically structured, consisting of linked rigid elements representing segments of the body [52]. These tend to be somewhat less flexible in their application, as animals vary greatly in their morphology. In addition, the complexities of biological systems, and therefore that of anchor models, make them difficult to model and nearly impossible to fully explore their parameter space. In this thesis, template models are used to explore friction's effect on bipedal locomotion.

2.5.3 Spring-Loaded Inverted Pendulum (SLIP)

Many legged animals and robots move in a manner resembling a monopod bouncing along: measurements taken during steady locomotion from species varying widely in morphology and size reveal net center of mass (CoM) forces and trajectories remarkably similar to those of a pogo-stick, or more precisely, a point-mass atop a passively-sprung massless leg [13]: see Figure 2.13. This is referred to as the spring-mass model of locomotion, or more formally as the spring-loaded inverted pendulum (SLIP). The SLIP model (Figure 2.14) describes translation dynamics in the vertical plane (which coincides with the fore-aft sagittal plane since it implicitly assumes that no out-of-plane rotations occur). It consists of a point mass 'body' atop a massless passively sprung leg, a frictionless pin-joint hip, and a frictionless pin joining the infinitesimal point-foot at the end of the leg to the ground. A stride of SLIP is composed of a stance phase, liftoff event (LO), flight phase, and touchdown event (TD), after

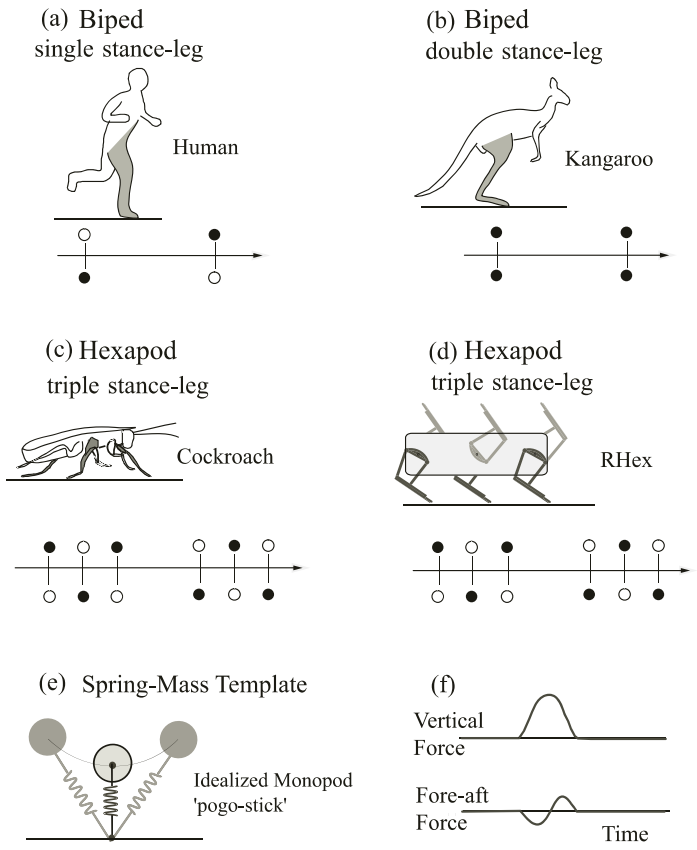

Figure 2.13. Animals and robots ranging in leg number and structure produce similar net ground force patterns. (a) A biped (human) with an alternating single leg stance. (b) A biped (kangaroo) with a double leg stance: a hopping gait. (c) A hexapod (cockroach) with alternating triple leg stance: a double tripod gait. (d) A hexapod robot (RHEX) with a double tripod gait. (e) The spring mass model of locomotion, a template for the steady-state motions of (ad). (f) Typical ground reaction force patterns of the systems in (ae). Reproduced from [14].

which the process repeats (Figure 2.14). Only conservative spring and gravitational forces act on the body, so the total system energy is conserved.

SLIP is a useful model in its convenience; it has only three parameters so it is easily studied. However, because it is energy-conserving, it is not useful as a biological model. It also has been shown that SLIP is not a stable model in biologically relevant parameter space, which means that while a lot can be learned about the model, how

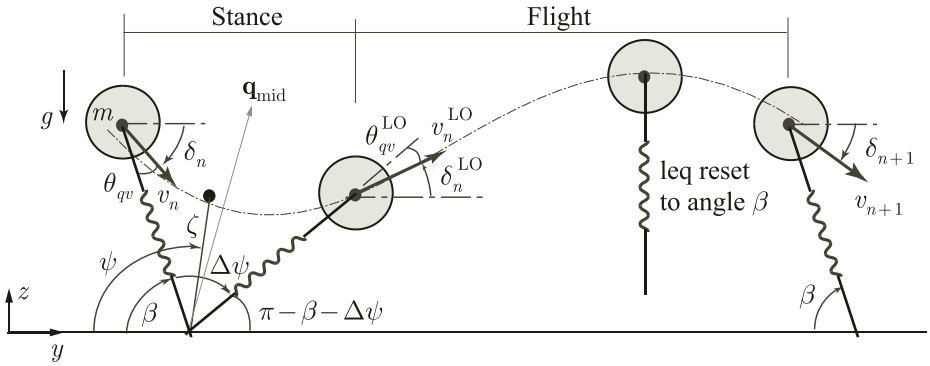

Figure 2.14. The SLIP model is the basic template model, a massive body on a massless spring leg. Reproduced from [14].

animals actually move cannot be learned from the model [16]. Despite this, work is still done with SLIP because it is a familiar and well understood model, and it offers a good reference with which to analyze other walking models (as in [53, 14]).

2.5.4 Robotic Hexapod (RHex) Platform

In parallel with the development of template models to accurately describe biological locomotion, researchers have also been moving forward with biomimicry of legged biological systems. This is the case with RHex, a hexapod robot inspired by research on cockroach locomotion [54, 55] with its sprawled posture, lower center of gravity, passive compliant legs, and clock-driven tripod gaits [56]. RHex can be seen in Figure 2.15.

These biologically motivated ideas, combined with sound scientific and engineering principles, have endowed RHex with a large repertoire of gaits, including walking over highly broken and irregular terrain [56], pronking (lifting all four feet off the ground simultaneously) [58], stair climbing [59], flipping [60], quadrupedal bounding [61], and even bipedal locomotion [57]. The high adaption rate of biologically inspired legged

Figure 2.15. The Robotic Hexapod (RHex) in a rock field. Reproduced from [57].

locomotion robots, such as RHex, has created a de-facto need for more physically sound models to predict their behavior.

2.5.5 Clock Torqued Spring-Loaded Inverted Pendulum (CT-SLIP)

Several models have been written as attempts at making a biologically-sound departure from the SLIP model, including the Clocked-Torque SLIP model (CT-SLIP) (Figure 2.16), which adds damping to the leg and a clocked torque at the hip, which provides energy input [52]. This model has found favor among those who seek to produce robots that spin sprung legs around a motor shaft as a means of propulsion [62, 63]. This is a practical model for that very reason; legs are easily attached to a revolving shaft, so a walking model that mimics biological walking but uses behaviors that are easily produced with electric motors is a very welcome model in the robotics community. Although the SLIP model can reproduce steady running behaviors of many animals and robots, it often fails to capture their dynamic stability. The CT-SLIP model develops a qualitatively correct and quantitatively-close model, which better estimates legged locomotion and provides sufficient predictive power for robot control on a stride-to-stride time scale, with added effects that appear capable of adequately capturing the robust properties of typical animal and robot running. The

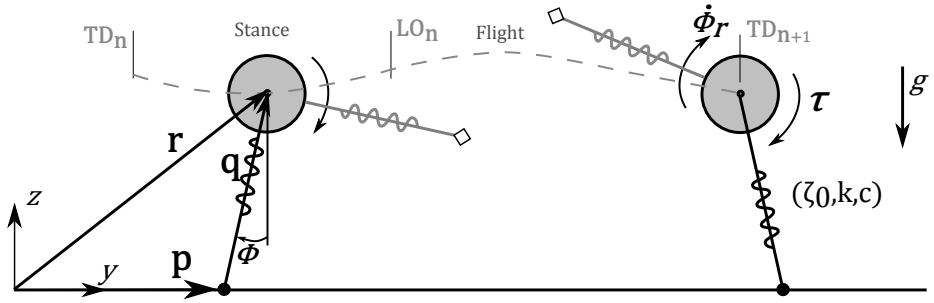

Figure 2.16. Legs in the CT-SLIP model follow a clock signal and a torque is applied to them in proportion to the amount the leg lags behind the clock. This model is especially useful for controlling legged robots with rotary legs. Adapted from [52].

CT-SLIP model was specifically developed to create a quantitatively better model of the behavior of legged robots such as RHex.

The CT-SLIP model does not directly incorporate friction into the dynamics of the leg motion; instead the model uses the standard stick-slip friction model, $F_{friction} = \mu N$, as a lift-off (LO) condition for the legs in the stance phase. By varying the friction coefficient, μ, the forward dynamics of the model can be greatly altered, as seen in Figure 2.17. Though modifying the LO condition improves the model's predictive power, it still remains short of quantitatively accurate results. An expansion of the CT-SLIP model to include foot slipping friction is explored in Chapter 5.

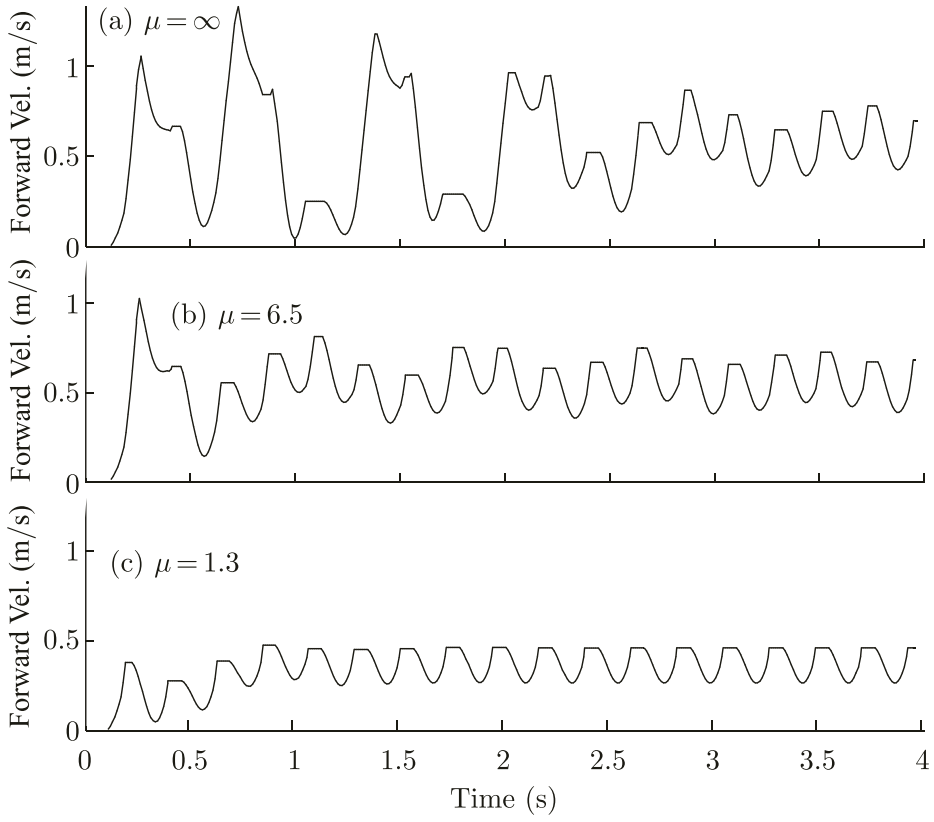

Figure 2.17. CT-SLIP comparison with varying stick-slip friction LO conditions. (a) $\mu = \infty$. (b) $\mu = 6.5$. (c) $\mu = 1.3$. Reproduced from [14].

3. MAPPING THE MINIMAL SKIN STRAIN VECTOR FIELD OF THE HUMAN BODY

This chapter introduces an improved technique for mapping the lines of minimal skin strain along the human body. The technique directly identifies the strain field on a subject, enabling immediate verification testing of various orthotic concepts based on minimum skin strain. This technique enables the development of passive joint parameter models in Chapter 4.

In this chapter, Iberall's protocol as described in Chapter 2 is improved upon to gather the lines minimal skin strain along the human body, simplifying the process and digitizing the data. Though the method provides only the direction of minimum skin strain and not the strain magnitude as in other methods [10,11], it directly marks the information on a subject's skin. This enables the development of joint models for various orthotic concepts based on minimum strain, a major intent of this thesis discussed in Chapter 4.

The techniques described in Chapters 3 and 4 have been developed in collaboration with A. Cherian and are awaiting publication [64]. The procedures and experiments described have been approved by the Purdue University Institutional Review Board (IRB) under the study titled "Evaluation of minimal skin strain vector field." For additional information regarding the approval, please reference IRB protocol #: 1302013190.

3.1 Strain Circle Theory

The theory used to identify the skin strain vector field is that of physical elasticity. Deformations in an elastic body are described by the strain ellipse, under which a small circle of material under elastic deformation deforms to an ellipsoidal shape [9].

The premise in identifying the skin strain vector field is that a small circle on the skin surface undergoing elastic deformation will deform to an ellipse. Superimposing the original circle back on the ellipse will reveal one of three possible cases, shown in Figure 3.1(a)-3.1(c). Since all points on the ellipse are derived from points on the non-deformed circle, in general, there will be two diameters of unchanged lengths, albeit with some rotation, indicated by the intersecting arcs. These Lines of Non-Extension (LoNE) exist at an offset angle, φ, from the line of maximal extension and are shown in Figure 3.1(a). LoNE do not always exists as the body moves, especially close to the joints. In these regions, lines of minimum compression and extension can be identified, as shown in Figure 3.1(b) & 3.1(c) [9]. Due to practical limitations of the measurement technique, a fourth case exists where the amount of skin deformation is too small to be identified and is therefore recorded as negligible deformation, as shown in Figure 3.1(d).

If measured at the extremes of deformation, it is assumed that the indicated minimal skin strain directions will be representative of the intermediate strain as well, as indicated in a previous study [9, 3, 10, 11]. By creating a grid of these strain circles, or nodes, on the body, one can map the directions of the skin strain vector field along the human body. By extending and connecting these directional nodes, the contours of minimum or non-extension can be mapped onto the skin surface.

3.2 Method

3.2.1 Strain Circle Method / Application

To establish a working protocol in gathering the strain ellipses, efforts were focused on the leg, extending from the thigh to the upper foot. This region spans the knee, a joint that predominantly has a single degree of freedom, significant range of motion that is greater than $90deg$, and ease of accessibility with modest clothing on the subject. Additionally, this region of the leg has been covered in several previous studies [15, 3, 10, 11] allowing for comparison to published results.

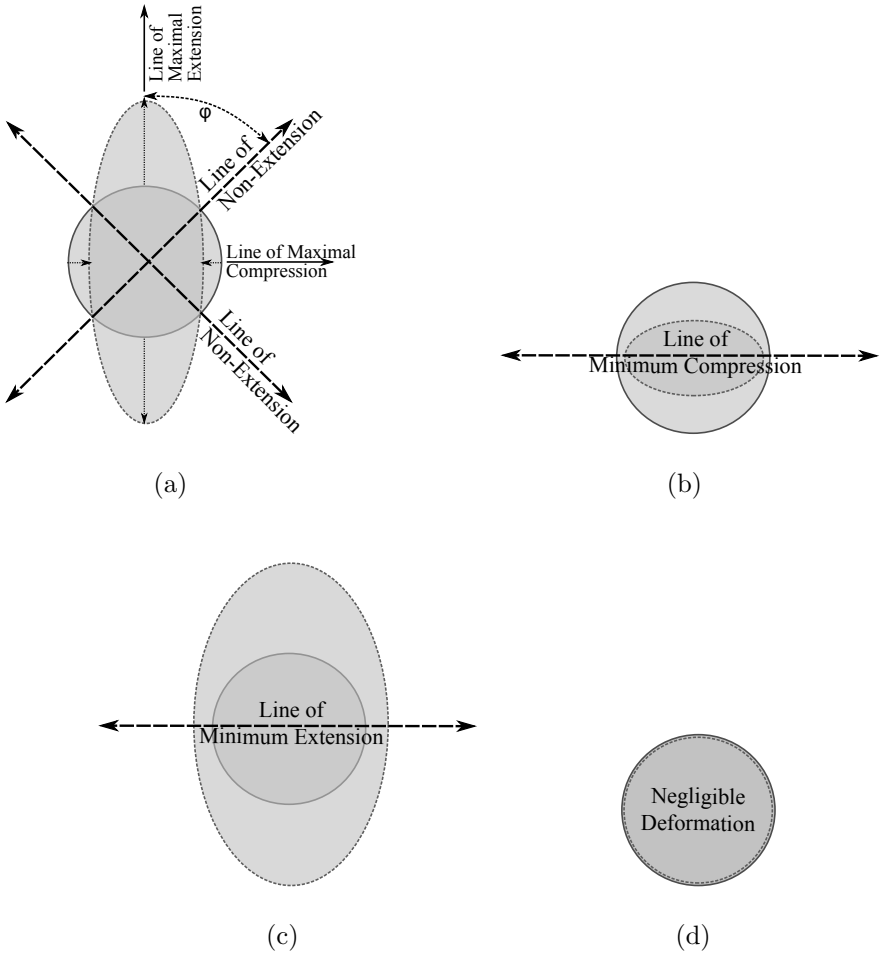

Figure 3.1. Possible skin strain circle patterns under elastic deformation: (a) Lines of Non-Extension, (b) Line of Minimal Compression, (c) Line of Minimal Extension, (d) Negligible Deformation.

Two leg positions at the extremes of joint range of motion were chosen to capture the typical skin strain during most tasks and activities of daily life, i.e. walking and sitting. The reference position consisted of the knee at full extension and the ankle at full plantar flexion and nominal eversion. The deformed position consisted of the knee held in flexion ($\varphi = 80deg$, to expose additional skin anterior of the knee) and the ankle at full dorsiflexion and nominal eversion. The representation of the capture positions can be seen in Figure 3.2.

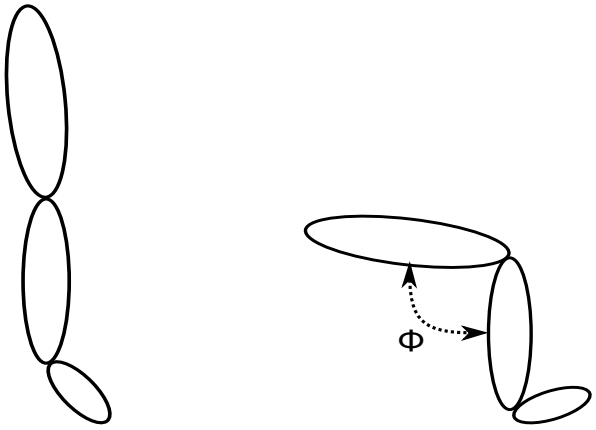

Figure 3.2. Capture Positions for strain detection: (a) Reference Position, (b) Deformed Position.

A regular grid of nodes was drawn on the subject's leg spanning the region of interest. Grid spacing was influenced by practical limitation of the method; larger spacing allows for easier to identify deformations; however, it reduces the data density. The minimal spacing was limited by the motion capture system and is discussed later. A dotted grid, approximately spaced at $1.25in$ by $1.25in$, was chosen as optimal for both data density and ease of application and was traced onto the subject's leg. Application of circles to the subjects was facilitated through the use of a custom stamp and non-toxic ink. The stamp consists of a 1 inch diameter ring and a centering point.

The strain circle application procedure is as follows:

1. With subject in reference position, mark each grid node with a circle using the stamp and a non-toxic ink pad
2. Have the subject move to the deformed position
3. Remark the grid nodes with a circle using the stamp and a different color ink, focusing on having the stamp centered on reference position's center dot

4. Mark applicable strain lines as described in Figure 3.1

This procedure is graphically depicted in Figure 3.3.

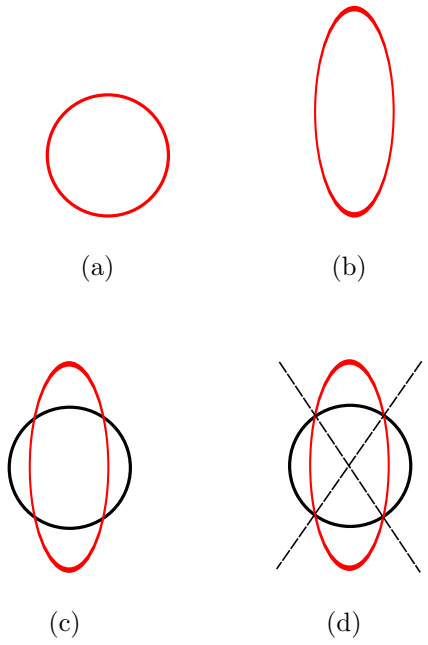

Figure 3.3. Strain Circle Application Procedure: (a) Draw Circle, (b) Deform Circle, (c) Original Circle Overlaid, (d) LoNEs Drawn.

3.2.2 Digital Capture

In order to digitally capture the skin strain vector field data, a technique was developed utilizing both a motion capture system and photogrammetry to digitally recreate the minimum skin strain vector field along with a 3D representation of the subject's leg. A four-camera Vicon (Vicon Motion Systems, Centennial, CO) motion capture system (MX-T160 cameras, 120 Hz, 16-mega pixel resolution), was used to track 6mm diameter circles of reflective tape (3M 7610) positioned on the skin.

Skin Strain Marking

A system for uniquely marking minimum strain direction of each of the four elastic deformation cases, shown in Figure 3.4, was created. Figure 3.4(a) shows the LoNE case with three markers, one on the origin and one on each of the LoNE vertices. The cases of minimum compression and extension, shown in Figure 3.4(b-c), each use two markers to indicate the minimum strain direction. The node's origin in these cases can be recreated by averaging the marker's position. Figure 3.4(d) shows the negligible deformation case with a single marker.

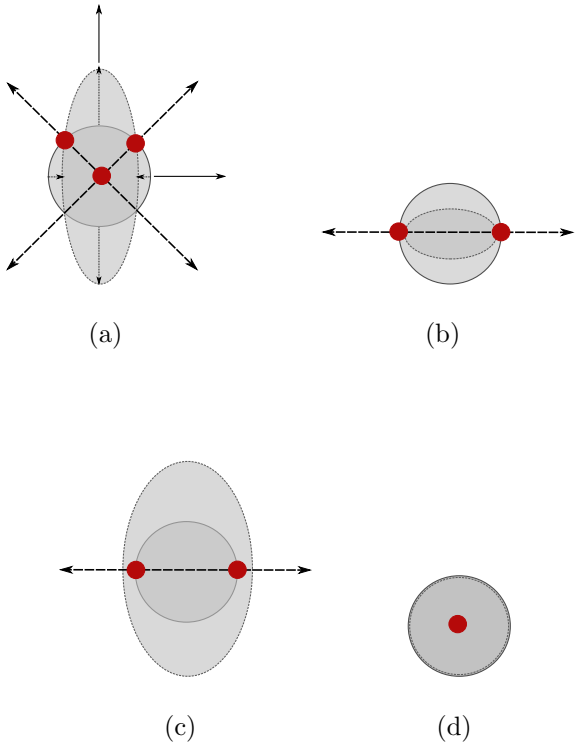

Figure 3.4. Skin strain circle cases with motion capture markers (red circles) applied: (a) LoNE case, (b) Minimal Compression case, (c) Minimal Extension case, and (d) Negligible Deformation case.

Motion Tracking System

Flat tracking markers can be applied directly to the skin surface, removing offset errors inherit in the standard Vicon spherical markers. Using the proprietary Vicon capture software, testing showed the markers required a minimum spacing of $0.4in$ and less than a $70deg$ incidence angle to be detected reliably. Additionally, the motion capture system requires a marker be seen by a minimum of 2 cameras to detect and track each marker's position. Considering the curvature of the leg and the maximum incidence angle of the markers, it was not possible to capture all of the leg markers at the same time. Instead, a series of snapshots were taken of the subject and then digitally stitched together. To insure consistent subject stance throughout all of the snapshots, a structure mounted on a large radial bearing (commonly known as a lazy susan) was created for the subject to stand on. The subject was able to rest on the structure while it rotated, thereby insuring consistent marker positions between captures. Snapshots were taken at approximately $22.5deg$ intervals around the subject; after a one second snapshot was captured, the stand was rotated to the next position. As an orientation tool between the snapshots, seven markers were placed in an easily identifiable configuration at the bottom of the stand. The capture setup can be seen in Figure 3.5. A dedicated analysis program was created for stitching the snapshots together from position data using MATLAB (MathWorks, Natick, MA). Using the orientation markers located on the structure in each snapshot, three common markers were selected between the first snapshot and each remaining snapshot. An orthogonal reference coordinate system $(\vec{E}_1, \vec{E}_2, \vec{E}_3)$ was created in the first snapshot using the three markers (A, B, C). Then an orthogonal local coordinate system $(\vec{e}_1, \vec{e}_2, \vec{e}_3)$ was created in each remaining snapshot using the corresponding markers (a, b, c). Each marker, m_{ij}, in a snapshot was then projected onto the local coordinate system using

$$\vec{n}_{ij} = \frac{\vec{m}_{ij} \cdot \vec{e}_1}{\vec{e}_1 \cdot \vec{e}_1} \vec{e}_1 + \frac{\vec{m}_{ij} \cdot \vec{e}_2}{\vec{e}_2 \cdot \vec{e}_2} \vec{e}_2 + \frac{\vec{m}_{ij} \cdot \vec{e}_3}{\vec{e}_3 \cdot \vec{e}_3} \vec{e}_3 \,. \tag{3.1}$$

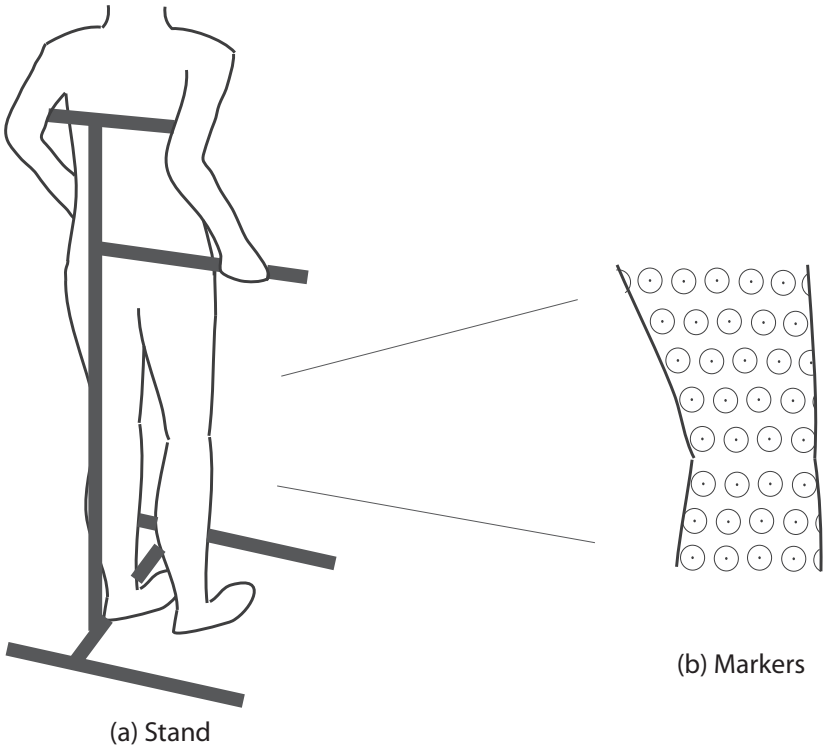

Figure 3.5. Vicon Capture Test Rig. The capture test rig for the Vicon system can be seen in (a). The marked strain circles can be seen in (b).

Using the projected lengths, the markers were then projected onto the reference coordinate system using

$$\vec{N_{ij}} = \vec{O} + (n_{e_1}\,\vec{E_1} + n_{e_2}\,\vec{E_2} + n_{e_3}\,\vec{E_3}), \tag{3.2}$$

where $\vec{O}$ is the norm between origins in the reference coordinate system. Following the stitching algorithm, several redundant markers existed due to the large number of snapshots. This marker redundancy was accounted for by digitally removing markers closer than a distance threshold below the minimum marker spacing. The resulting stitched marker data can be seen in Figure 3.6. The markers identifying a node, based on the system shown in Figure 3.4, were then reselected and the corresponding lines of minimum strain plotted. The resulting skin strain vector field can be seen in Figure 3.7.

Figure 3.6. Representative point cloud of stitched marker data.

Photogrammetry

After taking the snapshots with the motion capture system, digital photos of the leg were taken to reconstruct the leg contours using photogrammetry. 123D Catch (Autodesk, San Rafael, CA), a free cloud based photogrammetry service, was used to reconstruct a mesh of the subject's leg. In order to reconstruct the contour of the subject's leg, 76 pictures were taken of the leg. The subject remained on the motion capture structure so as to hold completely still, and pictures were taken while the photographer rotated around the leg.

For the first rotation around the leg, the whole leg was in focus. In sequential rotations, the lower and upper halves of the leg were the focus of the pictures. At parts of the leg where there is a steep contour, such as the heel, more pictures were taken. This increases the likelihood that the pictures are stitched together in the

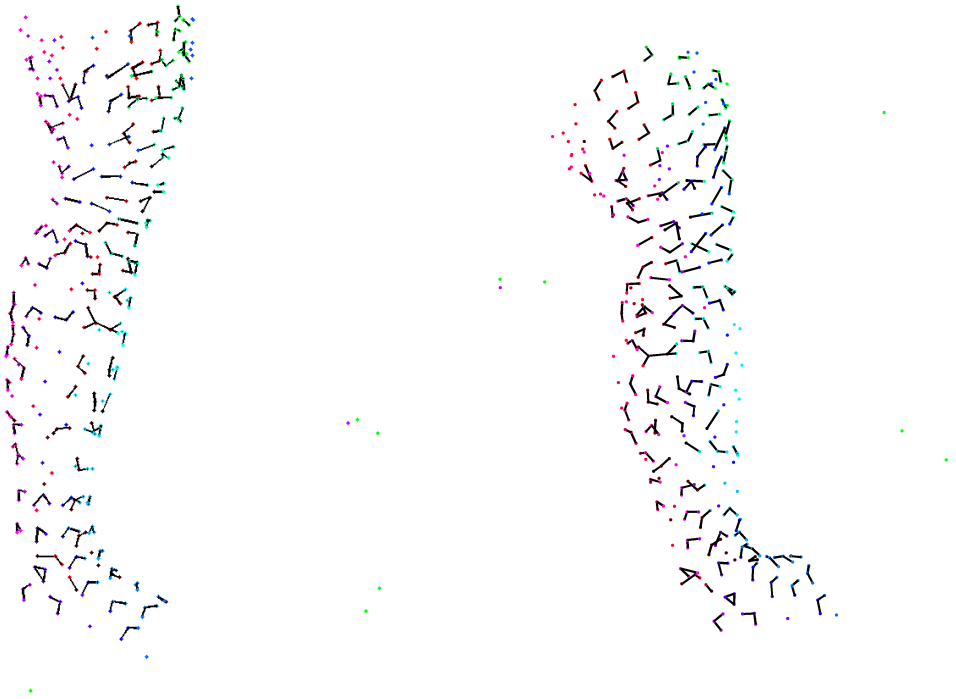

(a) (b)

Figure 3.7. Representative skin strain vector field: (a) Anterior-lateral perspective, (b) Posterior-lateral perspective

photogrammetry software, which will be explained shortly. A soft, white light was added to the inside of the knee reduce shadow in that area.

These photos were then uploaded into 123D Catch. This particular program takes one photo of the object and then finds three unique points that are common between it and the photo before and after it. Because the photos are taken in a circular path, the points will have moved slightly. Depending on how far these points are displaced, the program will create a surface to match the slope of the object in the photo. The resulting surface can be seen in Figure 3.8.

After reconstructing the 3D surface of the leg, it was exported as a surface mesh (*.obj*) for further use.

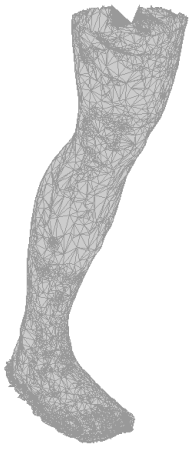

Figure 3.8. Representative photogrammetry reconstruction.

Merged Data Sets

The 3D surface mesh was imported into MATLAB and three common points were identified between the mesh and marker data. Using the previously explained algorithm, the surface mesh was scaled and superimposed onto the marker point cloud. Superimposing the two datasets added spatial context to the skin strain vector field and provides a more intuitive understanding of how the vector field flows along the subject's leg. The merged data set can be seen in Figure 3.9. In addition to adding spatial context to the skin strain vector field, the 3D mesh can also assist in sizing considerations for orthotics based on the LoNE principle.

Skin Strain Contours

The skin strain vector field shown in Figure 3.9 gives the information required to estimate skin strain contours on the analyzed skin region. A selection algorithm was programmed in MATLAB that allowed LoNE contours to be manually drawn

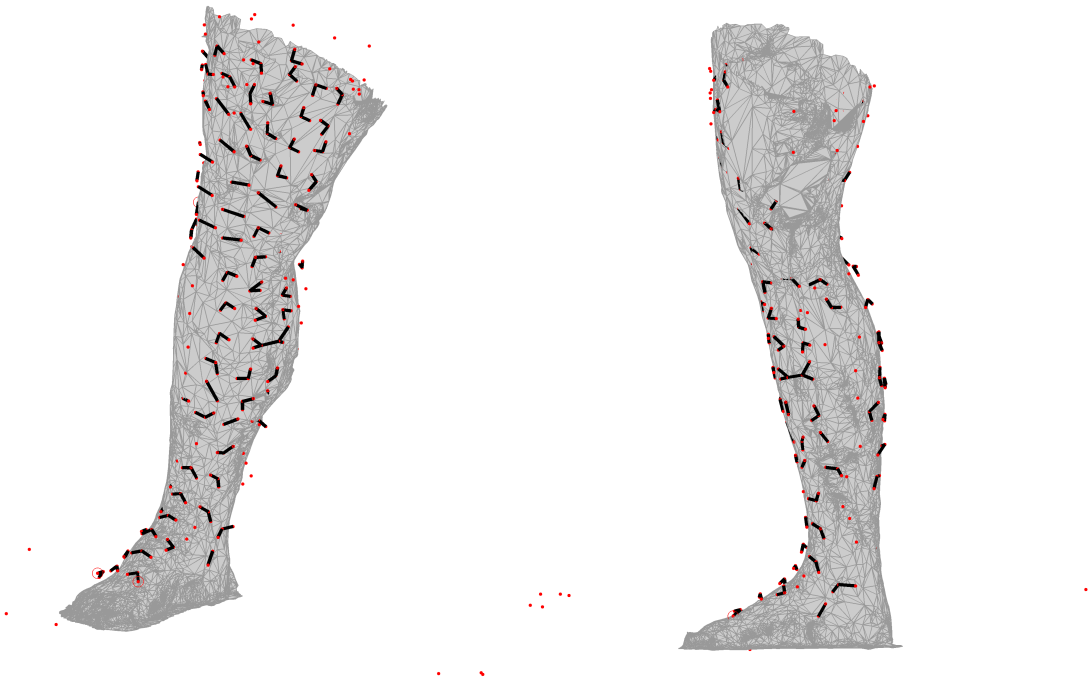

(a) (b)

Figure 3.9. Representative 3D surface mesh with overlaid skin strain vector field: (a) Anterior-Medial view, (b) Posterior-Medial view.

by linking successive skin strain vector nodes. The nodes were selected taking into account the local minimum skin strain directions and the direction of neighboring nodes. Two such LoNE contours are shown in Figure 3.10. Automatic algorithms for linking LoNE contours were investigated; however, they were deemed insufficient for accurately extrapolating the contours. Following current best practice [3, 10, 11], the skin strain vector nodes were manually interpolated, taking into account the vector information of distant nodes, and the proper path through gaps in the vector field determined. These limitations may be overcome with a denser vector map allowing for closer node connections.

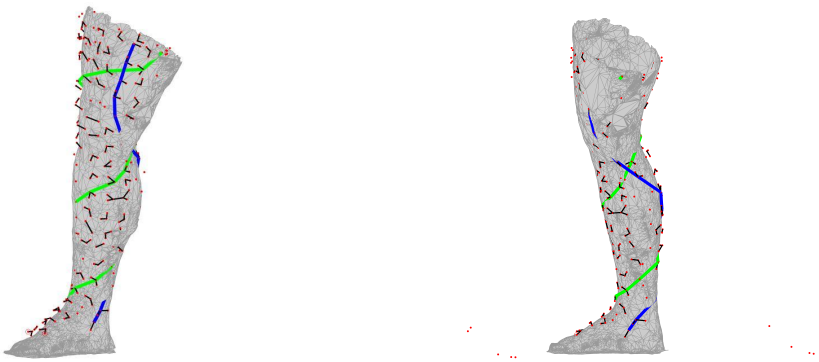

(a) (b)

Figure 3.10. Representative 3D surface mesh with two overlaid LoNE contours in blue and green: (a) Anterior-Medial view, (b) Posterior-Medial view.

3.2.3 Limitations

The ability to identify LoNE and minimal strain lines is greatly impacted by the line thickness of the stamp, thicker lines obscure strain, and the alignment of the center points, offsets can lead to unidentifiable intersection points and minimal strain vectors. Care must be taken during application of the circles to minimize corrupted data nodes.

On visual comparison between the digitally captured markers and digital photographs, the motion capture system failed to pick up all the markers. This is due, in part, to the limited reflectivity of a flat circular disc of reflective tape when compared to spherical markers. Hemispherical domes covered with reflective tape are being tested to improve marker identification by improving the marker's incidence angle. Additional motion capture cameras would eliminate the need for taking snapshots and merging the markers together, eliminating a significant source of error.

Lastly, the current photogrammetry software requires the data to be uploaded to a commercial cloud server for processing. In light of maintaining full ownership of

experimental data, there is a need migrate to a locally processed photogrammetry software like Visual Surface from Motion, CMMS, or PMVS.

3.3 Discussion

A new technique is presented for mapping and digitally capturing the skin strain on a human subject. This new technique improves upon Iberall's method [9] by presenting a simplified strain ellipse application process and a method for digitally capturing the location and direction of the LoNE, minimum extension, minimum compression, and negligible deformation nodes along with the complex contours of the leg. It provides an alternative technique to previous studies [3, 10, 11] that allows for direct testing of minimum skin strain contours as a structure for conformal orthotics.

Further study is required to determine the feasibility of using this new technique to map the skin strain vector field. In addition, the skin strain vector field needs to be mapped across additional subjects to develop a subject invariant topological map of the skin strain vector field of the human body.

4. VERIFYING THE MINIMAL SKIN STRAIN VECTOR FIELD BASED ORTHOTIC WRAPS

This chapter explores the various possible orthotic wraps that can be aligned to the skin strain vectors and provides a modeling tool to study the effect conformal orthotic structures on the passive joint parameters of the knee. These joint parameters can then be used for predicting how conformal orthotic structures will effect a human task, such as locomotion.

The technique described in Chapter 3 provides a visual identification of minimal skin strain directions on a subject. This skin strain map can then be used to develop conformal orthotic wraps that align with the skin strain vectors. This chapter explores the various possible orthotic wraps and develops a modeling tool for studying the effect conformal orthotic structures on the passive joint parameters of the knee. Using these modeled parameters, the alignment of the orthotic wrap to the skin strain vectors can be varied to tune the effect of a conformal orthotic structure on a subject. Furthermore, these joint parameters can be used for predicting how conformal orthotic structures will effect a human task, such as locomotion, a concept explored in Chapter 5.

4.1 Skin Strain Based Orthotic Wraps

The skin strain map technique detailed in Chapter 3 allows for the interpolation of LoNE contours on the surface. Following established practices [3,10,11], a skin strain contour can be created by linking successive skin strain vector nodes. By placing material along these contours, a series of orthotic wraps were developed that allow for immediate verification testing.

Table 4.1.

Selected Subject.

Age	25
Gender	Male
Height (m)	1.78
Leg Length (m)	0.42
Weight (kg)	92.8

4.1.1 LoNE Wrap

Taking into account the direction of minimum skin strain vectors in the immediate area, the LoNE can be extended from a node to its neighbors. By continuing this process across the entire mapped surface, LoNE can be drawn that extend across the entire leg. The LoNE drawn on the skin can then be directly used for wrapping orthotic test structures. Following the technique outlined in Chapter 3, a strain field was applied to a subject for conformal orthotic wrap evaluation. Information regarding the test subject can be found in Table 4.1.

When joining the skin strain vectors to form lines, high strain areas, i.e. above and below the patella (knee), can be interpreted to wrap around a segment or continue on to the next segment i.e, from the thigh to the leg. In other words, LoNE can be interpreted to span joints or terminate at them. Using the drawn LoNE as guidelines, two wraps were applied to the subject, the first with LoNE spanning the knee on one leg and the other terminating at the knee on the other leg. A double-sided hook and loop strap, commonly known as Velcro, was used as it was axially inextensible compared to the skin and, being double-sided, it would attach to itself at the intersection nodes allowing for easy application.

When wrapping the strap in a segmental configuration, the wrap starts from the upper extremity of the thigh, comes down the thigh, wraps around the knee, and back

up the thigh. The leg is similar, starting and stopping at the ankle and wrapping around the knee. The segmental wraps overlapped around the knee. When wrapping the strap in a continuous configuration, the wrap starts from the upper extremity of the thigh, comes down the thigh, wraps the knee, proceeds down the tibia, wraps around the ankle, and then back up the leg. A visual inspection of the segmental and continuous wraps shows little difference, as seen in Figure 4.1. After applying the

Figure 4.1. Segmented (black) versus continuous (orange) leg wrap.

LoNE wraps, the subject walked ($\approx 0.5\frac{m}{s}$) for a short period ($< 5min$) to evaluate differences between the segmental and continuous wraps. Following this, the subject ranked the comfort and mobility of each wrap based on Table 4.2. With the segmental wrap, it was observed that the knee cap was primarily responsible for holding the strap in place. On flexion of the knee, the strap would slip off of the knee cap and become slack. Conversely, the continuous wrap was observed to stay in place throughout the same dynamic movements. The tension in the strap as it went from the upper thigh, across the knee, to the leg, and then back up the lower leg, maintained it in place across the knee joint and along the whole leg. The subjects qualitative assessment of the wraps can be seen in Table 4.3. Considering these initial findings, continuous LoNE wraps were used in the following tests.

Table 4.2.
Modified Corlett and Bishop discomfort and Cooper-Harper body control scale. Adapted from [65].

Rating	**Discomfort**	**Body Control (Mobility)**
1	Nude comfort	Unrestricted
2	Pajamas, casual clothes	Negligible deficiencies
3	Formal attire	Minimal compensation required
4	Minor discomfort if worn all day (16 h)	Minor but annoying deficiencies
5	Too uncomfortable to wear all day	Moderately objectionable deficiencies
6	Too uncomfortable for 8 h	Tolerable deficiencies
7	Too uncomfortable for 4 h	Maximum tolerable compensation required
8	Too uncomfortable for 2 h	Considerable compensation required
9	Too uncomfortable for 1 h	Intense compensation required
10	Too uncomfortable for 10 min	Body control lost

Table 4.3.
Selected subject rating of LoNE contours.

	Discomfort	**Body Control**
Segmental	5	4
Continuous	3	2

4.2 Wrap Fit Testing

One of the primary goals of using LoNE based orthotics is to create conformal orthotics that can move dynamically with the human body. To assess the feasibility of various wrap configurations, wraps were applied to a subject and a series of tests were performed to assess tension in the wrap throughout joint flexion and limitations to joint range of motion.

A test comparing conformity between the LoNE wrap and a Non-LoNE longitudinal wrap was performed. A subject's leg was wrapped with a continuous LoNE strap and two different longitudinal straps. The wraps were applied with the subject standing with full knee extension. The subject then flexed their knee to an approximately $90deg$ angle and the wraps were checked for tension. The contours can be seen in Figure 4.2 and Figure 4.3. The LoNE wrap was found to remain in its

(a) (b)

Figure 4.2. Conformity wrap test, contour 1. The nominal position can be seen in (a), the flexed position can be seen in (b).

applied tension through the movement. However, the longitudinal wrap was observed

(a) (b)

Figure 4.3. Conformity wrap test, contour 2. The nominal position can be seen in (a), the flexed position can be seen in (b), the stretched contour used to measure deformation can be seen in (c).

to develop significant slack during the movement, to the point of losing contact with the skin at many locations. The length of the longitudinal wrap was recorded and then its slack was removed and the wrap re-measured, providing an estimate of strain along the contour. These strain values can be seen in Table 4.4. These initial results suggest that LoNE based contours may make good candidates for devices seeking to conform to the skin's surface, remaining in contact throughout joint movements.

Table 4.4.
Longitudinal Contour Deformation.

	Contour 1	**Contour 2**
Flexed length	$30.8in$	$33.4in$
Stretched length	$30.3in$	$27.8in$
Deformation	1.6%	16.6%

4.3 Pendulum Test

As originally conceived, LoNE based suits were theorized to provide a structure conformal to the body that would offer no resistance to joint movement, a so called 'no-work' suit [9]. By offering no resistance, a 'no-work' suit would also allow full range of motion to the subject. An experiment to evaluate knee range of motion with alternative wraps was performed.

4.3.1 Method

Wartenberg's Pendulum Test of the leg [12] was used to determine the passive properties of the wraps. A drop test, from full knee extension to neutral flexion point, was conducted with various orthotic wraps. Three different configurations were tested: a subject with no wrap (control), a LoNE based wrap, and a longitudinal wrap along with the ventral side of the leg (Non-LoNE). The wraps can be seen in Figure 4.4. After applying a given wrap to the subject's leg, motion capture markers were applied to the subject's leg at the hip, knee, and ankle. The subject then laid down on a table with their knee and lower leg extending over the edge. After relaxing the leg muscles, the subject brought their knee to full extension. When ready, the subject indicated to the investigator to start the trial and then let their muscles go slack and their leg drop. The motion was tracked until the leg came to rest and the final leg

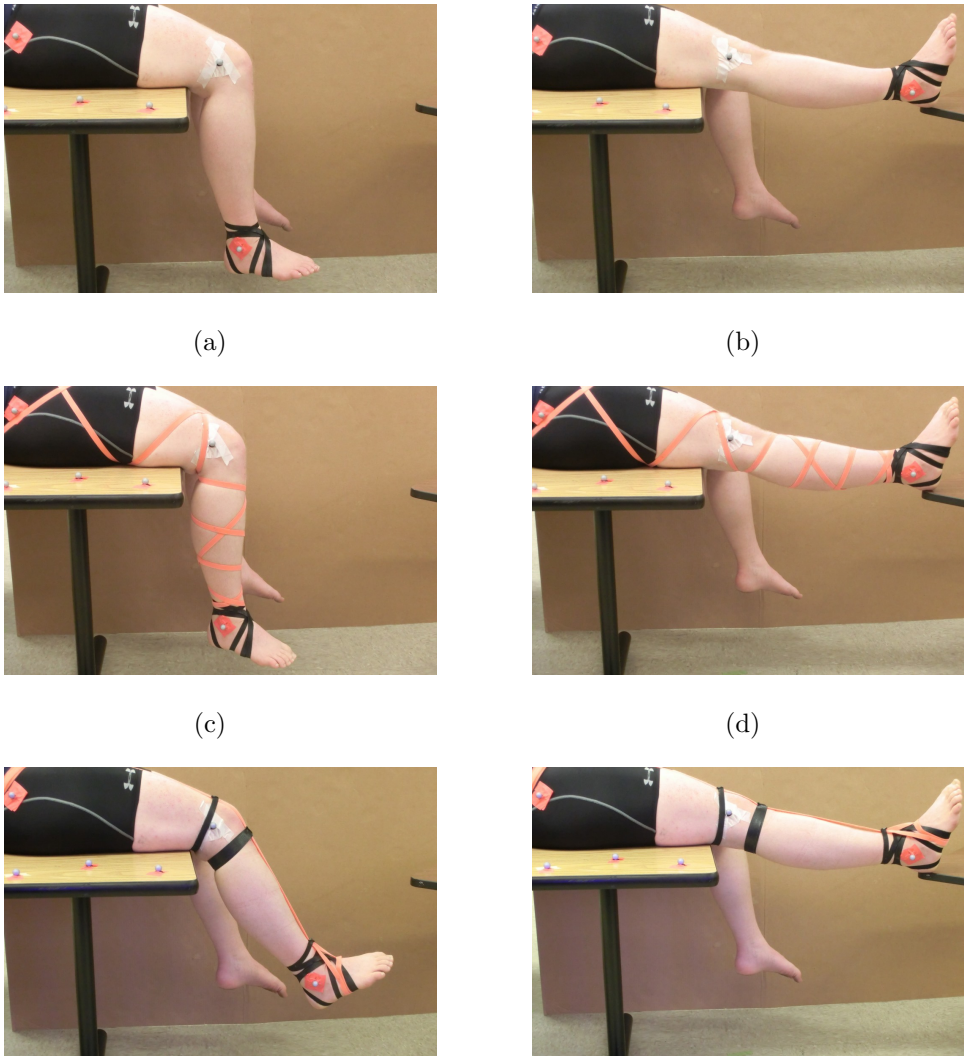

(a) (b)

(c) (d)

(e) (f)

Figure 4.4. Range of motion wraps for pendulum drop testing. Control is seen in (a-b), LoNE wrap is seen in (c-d), and Non-LoNE warp is seen in (e-f). Initial and final positions are shown for each test.

angle was recorded. For each wrap configuration, there were 10 pendulum drop trials conducted.

After completing the trials, the marker data was digitally filtered (6^{th} order Butterworth, low-pass, $f_c = 20Hz$) and the knee angle computed for each frame. The

filtered data was then corrected for phase offsets using a threshold angular velocity. The mean and standard deviation (σ) of the resulting aligned data was calculated and plotted with the individual trials to identify outliers. Data sets outside a $\pm 1\sigma$ window were excluded from further analysis.

4.3.2 Results

The resulting final flexion angles are shown in Figure 4.5. The base flexion angle

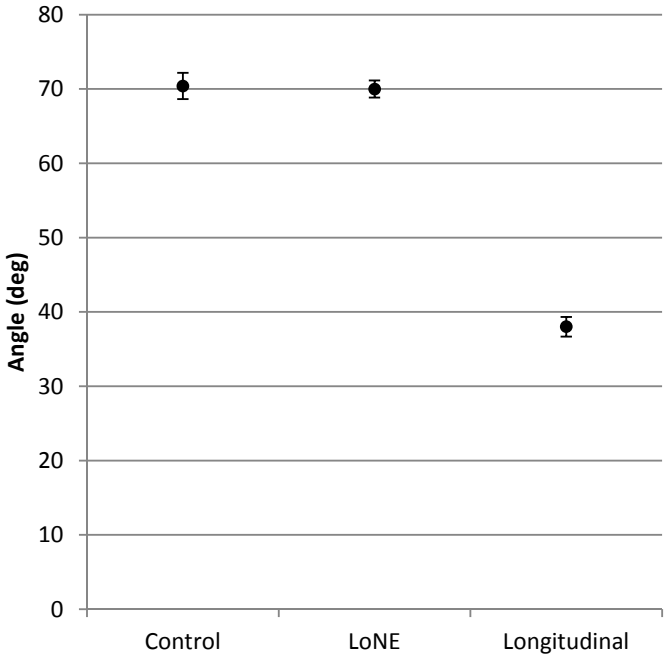

Figure 4.5. Final leg angle of static drop test.

found in the control experiment was found to be $70.4 \pm 1.8 deg$. The LoNE wrap was found to have flexion angle of $70.0 \pm 1.2 deg$, while the longitudinal wrap was found to have a base flexion angle of $38.0 \pm 1.3 deg$. These initial findings suggest that the passive properties of LoNE based wraps are similar to the bare leg and allow full joint range of motion.

The experimental results of the pendulum drop test can be seen in Figure 4.6. Initial observations reveal that the data is fairly consistent across trials. Both the control and LoNE wrap cases have 2^{nd} order dominate responses with light damping while the Non-LoNE case has a highly damped 2^{nd} order response. The control and LoNE cases both show flexion to approximately $100deg$ before settling; the Non-LoNE case has a peak flexion of approximately $35deg$.

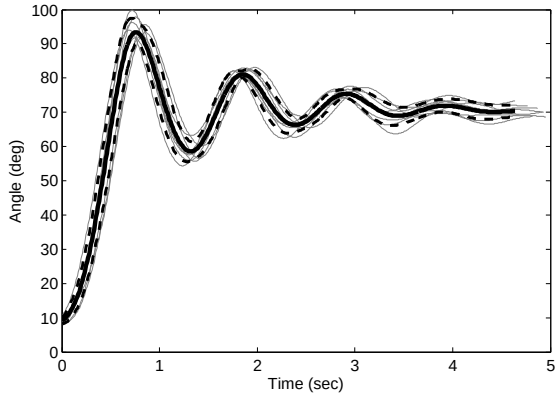

(a)

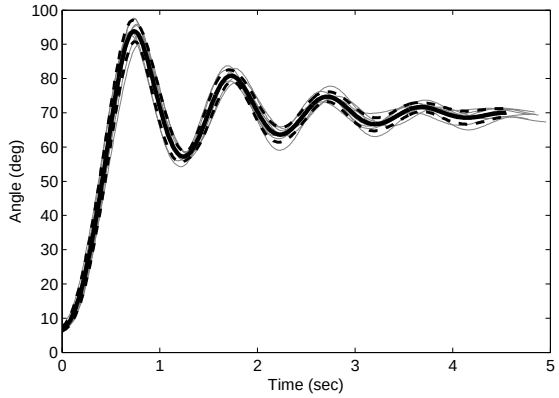

(b)

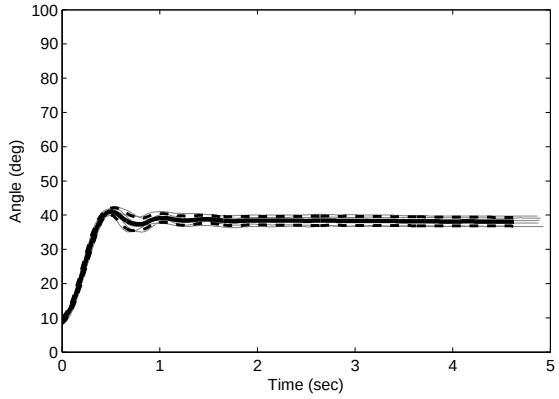

(c)

Figure 4.6. Experimental results of pendulum test. The individual trials are in light gray, the solid black line is the mean, and the dotted black lines are $\pm 1\sigma$. (a) Control, (b) LoNE, (c) Non-LoNE.

4.4 Dynamic Wrap Model Fitting

In order to better understand the results of the pendulum drop test, a model was developed to fit the data. The intent of the model is to extract passive knee properties from each experimental data set for comparison.

4.4.1 Model

Though the human body is chiefly comprised of non-linear materials and complicated joint interactions, it is generally held that the passive response of the knee joint can be described as a 2^{nd} order system [49]. This, combined with the initial observations made earlier of characteristically 2^{nd} order behavior of the response, lead to the initial use of a 2^{nd} order rotational system to model the data.

A free body diagram of the system can be seen in Figure 4.7. Working from first

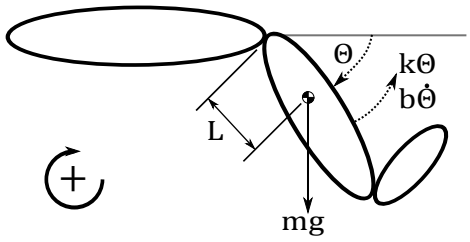

Figure 4.7. Free body diagram human leg model for pendulum test.

principles and the coordinate system shown in Figure 4.7, the equations of motion for the system can be written. The equations of motion for the 2^{nd} order rotational system with a linear stiffness are given by

$$I\ddot{\theta} + b\dot{\theta} + k\theta = Lmg\sin\theta. \tag{4.1}$$

Considering the non-linear nature of the human body and the potentially unknown dynamic effects of the LoNE and Non-LoNE wraps on the knee joint, a non-linear

Duffing model was also used in the data fit. The equations of motion for the 2^{nd} order rotational Duffing system with a cubic non-linear stiffness element are given by

$$I\ddot{\theta} + b\dot{\theta} + k\theta + k_c\theta^3 = Lmg\sin\theta. \tag{4.2}$$

In addition to the unknown stiffness and damping terms in each model, the leg's moment of inertia about the knee, I_p, the length from the knee to the leg's CoM, L_p, and the mass of the leg, m, are all unknowns. While many previous kinesiology studies have estimated the leg inertia and CoM with a homogenous rod model [49, 66, 67], a higher fidelity model was desired for this study. Using the combined foot and leg anthropometric data presented in Table 4.1 of [19], it is possible to calculate the model parameters (m, L_p, I_p) as follows:

$$m = 0.061M = 0.061(92.8kg) = 5.7kg, \tag{4.3}$$

$$L_p = 0.606L = 0.606(0.42m) = 0.25m, \tag{4.4}$$

$$I_p = m\rho_p^2 = (5.7kg)(0.42m * 0.735)^2 = 0.5503kgm^2. \tag{4.5}$$

4.4.2 Fitting Method

Fitting the models in Eqns. 4.1 and 4.2 to the experimental data was accomplished using a custom algorithm in Matlab. The overall structure of the algorithm is described in Figure 4.8. The model equations of motion are set up to be numerically

Model ⇒ Numerical Solver ⇒ Cost Function ⇒ Genetic Algorithm ⇒ Optimal Joint Parameters

Figure 4.8. Model fitting algorithm structure.

solved using the MATLAB function 'ode45' for a given set of stiffness and damping parameters. The output of the numerical solver is the angular position of the model over the specified time interval. This model output, θ_m, is directly compared to the

mean of an experimental data set, θ_e, at every time step using the sum squared error given by

$$error = \sum_i (\theta_{m,i} - \theta_{e,i})^2. \tag{4.6}$$

This calculated error value is used as the cost term for a parameter search. In this algorithm, a genetic algorithm (MATLAB function 'GA') is used to find the lowest cost combination of stiffness and damping parameters for a given set of experimental data. The process is then repeated for each data set (control, LoNE, and Non-LoNE) and each model (linear and Duffing).

4.4.3 Results

The best fit for each data set and the linear and Duffing models can be seen in Figure 4.9. The polynomial model optimized to nearly identical cost values and joint parameters as the Duffing system and was therefore not plotted here. The accompanying model joint parameters can be seen in Table 4.5 for the linear case and in Table 4.6 for the non-linear Duffing system.

Table 4.5.
Linear leg model fit parameters.

	Stiffness $(\frac{N}{rad})$	**Damping** $(\frac{Ns}{rad})$	**Error**
Control	3.71	1.47	3270
LoNE	4.13	1.48	5660
Non-LoNE	16.79	4.59	210

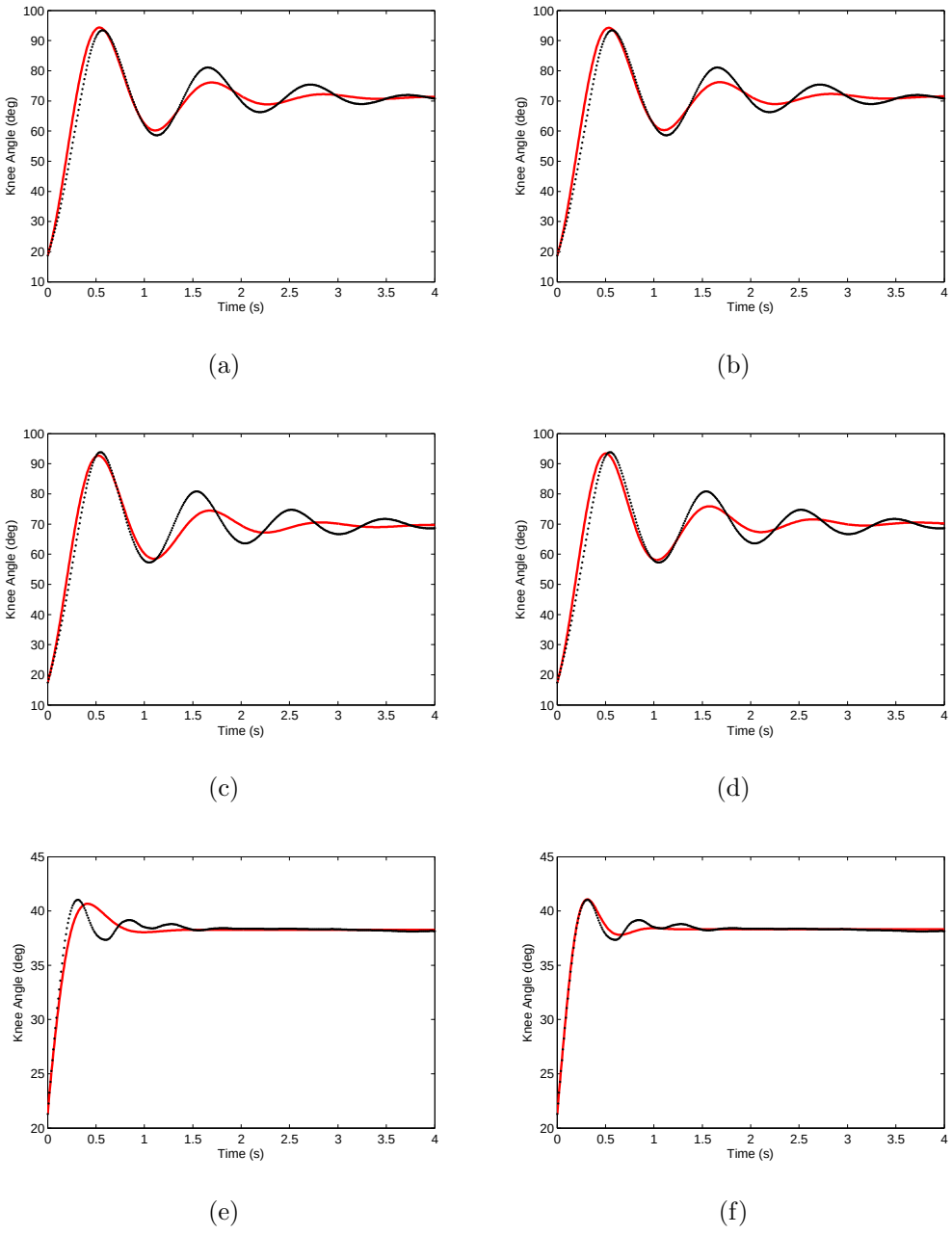

Figure 4.9. Dynamic Wrap Model fitting for pendulum drop test. Control is seen in (a-b), LoNE wrap is seen in (c-d), and longitudinal wrap is seen in (e-f). The linear model fit (left) and non-linear Duffing fit (right) are shown for each configuration.

Table 4.6.
Duffing leg model fit parameters.

	Stiffness	**Cubic Stiffness**	**Damping**	**Error**
	$(\frac{N}{rad})$	$(\frac{N}{rad^3})$	$(\frac{Ns}{rad})$	
Control	3.54	0.10	1.48	3240
LoNE	2.70	0.84	1.46	3830
Non-LoNE	0.00	37.42	5.47	30

4.5 Discussion

A verification experiment of wraps based on minimum strain contours was presented and indicated the wraps remain conformal to the skin through the body's motion and no significant reduction in the joint's range of motion was observed.

The three leg models were all successfully fit to the three experimental data sets. Despite the presence of non-linear elements in the experiments, the linear model of stiffness had a good fit for each of the data sets. The control data set (no wrap) was the best fit for the linear stiffness model. This is expected given the wide spread use of this model in kinesiology [49]. The linear stiffness fit of the LoNE data set is adequate; however, there are non-linear effects at work in the data set that the linear model is not capably of matching, such as an increase in damped natural frequency over time. The linear stiffness model manages to fit the Non-LoNE data set fairly well, only missing a good fit of the initial peak.

There are several trends in the linear stiffness leg model's joint parameters. As the wrapping becomes more restrictive, the effective joint linear stiffness and damping increase. The stiffness and damping values of the control and LoNE data sets are similar with an approximate 10% difference. However, the Non-LoNE set is approximately 4 times higher in stiffness and 3 times higher in damping. Furthermore, the

linear joint stiffness shown in Table 4.5 matches closely to the established value of $4.5\frac{N}{rad}$ cited by [68].

The Duffing leg model with cubic stiffness had the best fit of all the models on all three data sets. It closely matches the experimental data in all cases, doing notable better than the linear stiffness model as time progresses. Despite being the best fit of the leg models evaluated, the model is not able to perfectly predict the motion of the leg. While it does better than the linear model as time progresses, it begins to diverge toward the end of each trial. This may suggest additional dynamic effects in the leg that cannot be explained solely by passive elements.

Comparing the Duffing leg model joint parameters listed in Table 4.6, the damping follows a similar trend as with the linear model; the control and LoNE data sets have similar damping while the Non-LoNE set has a significantly higher value. The trends in stiffness are more difficult to characterize as there are two stiffness terms to be considered. As before, the Non-LoNE stiffness terms are significantly higher than the other data sets with the cubic stiffness term dominating the response. The control case has the least cubic stiffness, instead maintaining a larger linear stiffness value. The LoNE data set has a significant amount of both linear and cubic stiffness, though it has less linear and more cubic than the control. In all three models, the fit cost of the model was reduced as compared to the linear case. There are no known established joint parameters for Duffing leg models.

The linear stiffness of the control data set was validated against an established data set, indicating the joint parameters found through the modeling fit algorithm are reasonable. Significant differences in joint parameters were noted across different data sets, though most significantly between the LoNE based wraps and the Non-LoNE base wrap. This difference indicates that minimum skin strain based structures are more optimal than traditional orthotic structures. A further in-depth study is required to determine the feasibility of using this modeling technique to characterize conformal orthotic structures. Chiefly, for a given subject, the repeatability of joint parameters for a given wrap must be established and the model's ability to predict

motion with different initial conditions needs to be explored. Additionally, the resolution and practical limitations of the modeling fit need to be explored before using it to evaluate different configurations of contours across the skin strain vector field.

5. LOCOMOTION TASK MODEL

The design of any device requires an in-depth understanding of the task the device will be used for. By understanding the behavior of a given task, the system's design can be modified and tuned to improve its functionality and develop detailed design requirements. When designing a human interface design, this requirement is no less; however, understanding the task is typically more difficult [52]. The design of conformal orthotic devices for the lower extremities requires an understanding of how these device affect a given human task, such as locomotion.

Using the results of Chapter 4, modified joint parameters from a conformal orthotic structure could be applied to a locomotion model to predict the device's effect on locomotion. However, while many locomotion models have been developed to study legged locomotion [13, 14], apart from overall trend matching of trajectories and forces at steady state [13], little progress has been made in developing quantitatively accurate models. The need for better quantitatively predictive locomotion models needs to addressed before the effect of orthotic structures on locomotion can be studied.

Previous work on locomotion models has shown that friction at the foot interface plays an important roll in determining motion [14]. Despite this, most template locomotion models assume that there are no frictional effects on locomotion [16,13,53]. This chapter works to add friction as an important parameter in locomotion modeling to gain greater realism, as indicated by previous work [14].

5.1 Model Development

This section works towards expanding the CT-SLIP model to provide more accurate and predictable center of mass (CoM) motion by adding the ability for the feet

to slip while in stance. This model change can be seen in Figure 5.1. The addition of $\dot{p}$ to the model allows the legs to slide on the ground in response to forces in the leg.

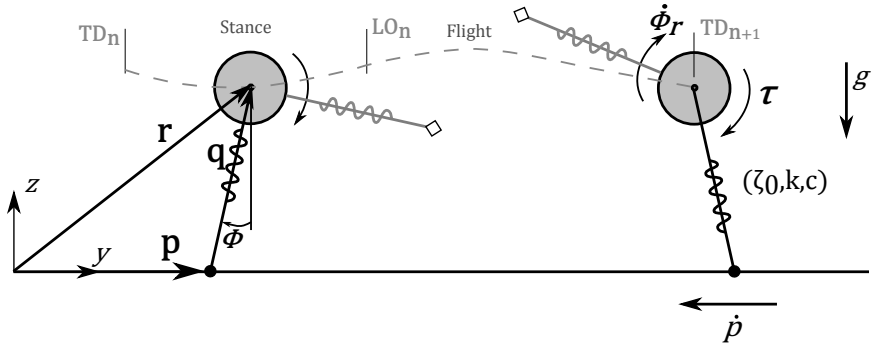

Figure 5.1. The CT-SLIP Model with frictional based foot slipping. Notice the $\dot{p}$ term added at the foot contact point.

5.1.1 CT-SLIP

As with SLIP, CT-SLIP is a hybrid system consisting of separate sets of equations for both the stance and flight phases of travel. Unlike SLIP, the CT-SLIP model is based on two legs rotating around a center of mass at the hip, which means there are four unique combinations of states. The equations of motion (EOM) for the flight phase are ballistic motion as the legs are massless constructs. Working from first principles and the coordinate system shown in Figure 2.16, the resulting governing equations for the flight phase are given by

$$\sum F_y = 0, \tag{5.1}$$

$$\sum F_z = mz := -mg. \tag{5.2}$$

Solving for acceleration yields

$$\ddot{y} = \dot{V}_y = 0, \tag{5.3}$$

$$\ddot{z} = \dot{V}_z = -g. \tag{5.4}$$

The equations of motion (EOM) for the stance phase involve modeling the forces in each leg as a simple linear spring and damper in parallel combined with a hip torque. The free body diagrams for the stance phase can be seen in Figure 5.2. Working from

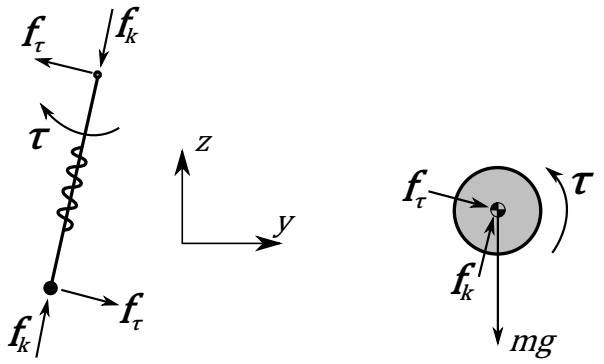

(a) (b)

Figure 5.2. CT-SLIP free-body diagrams for (a) a single leg, (b) and the rigid CoM/body. Adapted from [52].

the free-body diagram shown in Figure 5.2, the forces acting on the leg are given by

$$f_k = k(\zeta_0 - \zeta) - c\dot{\zeta}, \tag{5.5}$$

$$f_\tau = \frac{\tau}{\zeta}. \tag{5.6}$$

Working again from first principles and the coordinate system shown in Figure 5.2, the resulting governing equations for the stance phase in the Cartesian coordinate system are given by

$$\sum F_y = \left[k(\zeta_0 - \zeta) - c\dot{\zeta}\right]\left(\frac{y}{\zeta}\right) + \frac{\tau z}{\zeta^2} = m\ddot{y}, \tag{5.7}$$

$$\sum F_z = -mg + \left[k(\zeta_0 - \zeta) - c\dot{\zeta}\right]\left(\frac{z}{\zeta}\right) + \frac{\tau z}{\zeta^2} = m\ddot{z}. \tag{5.8}$$

Solving for acceleration yields

$$\ddot{y} = \left[\frac{k}{m}(\zeta_0 - \zeta) - \frac{c}{m}\dot{\zeta}\right]\left(\frac{y}{\zeta}\right) + \frac{\tau z}{m\zeta^2}, \tag{5.9}$$

$$\ddot{z} = -g + \left[\frac{k}{m}(\zeta_0 - \zeta) - \frac{c}{m}\dot{\zeta}\right]\left(\frac{z}{\zeta}\right) - \frac{\tau z}{m\zeta^2}. \tag{5.10}$$

The hip torque, τ, in Eqn. 5.6 is generated through proportional derivative (PD) control comparing the leg position, ϕ, to a reference leg position, ϕ_r, generated by a clock reference [14]. The clock reference is based on the *Buehler clock* originally developed for RHex [56] and can be seen in Figure 5.3.

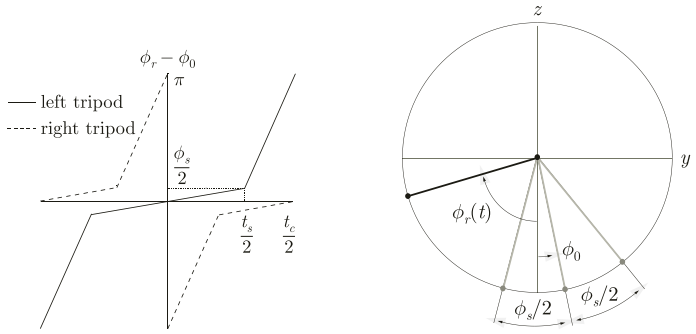

Figure 5.3. CT-SLIP reference clock for (a) desired leg angles vs. time, and (b) the corresponding desired leg configuration. Both (a) and (b) are defined by the clock parameters $(t_c, t_s, \phi_s, \phi_0)$ described in [14]. Reproduced from [14].

For simulation purposes, Eqns. 5.1 - 5.10 were rewritten in terms of the state vector,

$$x := \begin{bmatrix} y \\ z \\ V_y \\ V_z \\ p_1 \\ p_2 \end{bmatrix}, \qquad \dot{x} := \begin{bmatrix} V_y \\ V_z \\ \dot{V_y} \\ \dot{V_z} \\ \dot{p_1} \\ \dot{p_2} \end{bmatrix} = \begin{bmatrix} x(3) \\ x(4) \\ \ddot{y} \\ \ddot{z} \\ F_1 \\ F_2 \end{bmatrix}. \tag{5.11}$$

Where p_1 and p_2 are the feet positions as described in Figure 5.1 and F_1 and F_2 are functions governing the foot contact velocity.

5.1.2 Foot Contact Models

In CT-SLIP, foot contact is modeled as a pin joint with no slipping. A free body diagram of the CT-SLIP foot constraints is shown in Figure 5.4(a). In this model, the forces F_{Ny} and F_{Nz} can provide an infinite amount of force to restrain the foot to a single position, effectively making $F_1 = F_2 = 0$ in Eqn. 5.11. While this is a simplification of the system's dynamics, it has been observed that some biological systems with high dynamic stability have significant foot slippage while navigating uncertain terrains [55]. They utilize foot slippage to dissipate energy originating from disturbances, increasing their stability with open-loop controlled movements [69]. Mechanical systems have also demonstrated increased dynamic stability due to foot slippage [54]. With this in mind, the constraint forces used in the CT-SLIP model will be updated to frictional forces as seen in Figure 5.4(b).

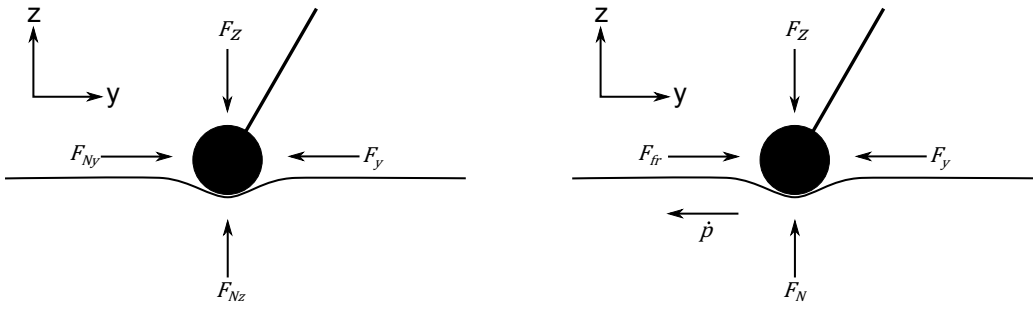

Figure 5.4. Foot contact interactions of (a) CT-SLIP and (b) model used in this study.

Following the example of advanced multi-body dynamic software [70, 71], this study will use the Stribeck friction model. The magnitude of Stribeck friction force can be calculated using

$$f_{friction} = \mu(v) f_{normal} \tag{5.12}$$

, where μ is a function of the slip rate, v, of which the general shape can be seen in Figure 5.5(a). For use in this initial investigation of contact dynamics, the friction coefficent will be approximated as linear, show in Figure 5.5(b).

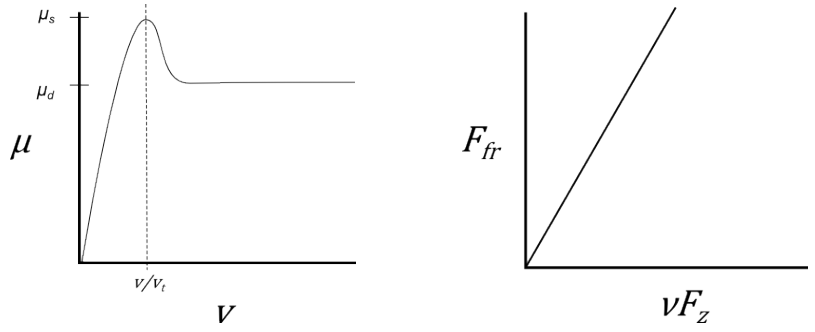

(a) (b)

Figure 5.5. Stribeck Friction described as a function of contact velocity. (b) shows a linear approximation of the beginning of the curved used in the foot contact model.

The Relative Force Friction (RFF) model was developed to have the contact force be a function of the normal force, F_z, proportional to the foot velocity. The force balance is given by

$$m\ddot{p} = F_y - b(F_z)\dot{p} = 0, \tag{5.13}$$

where $b(F_z)$ is the contact relationship as a function of F_z. The relationship used is given by

$$b(F_z) = (F_z + 1). \tag{5.14}$$

The final RFF model is given by

$$\dot{p_i} = F_i = -\frac{F_{y,i}}{F_{z,i} + 1}\alpha_{RFF}, \tag{5.15}$$

where $i = 1$ for the first leg and $i = 2$ for the second leg and α_{RFF} is a non-dimensional constant added for model tuning.

For the RFF model, α_{RFF} was varied between 0 and 1.5 to find an ideal value for quasi-periodic motion. This analysis is shown in a later section.

Table 5.1.

Model Parameters.

Constant/Parameter	**Value**	**Units**
g, gravitational constant	9.81	$\frac{m}{s^2}$
m, body mass	7	kg
ζ_o, unstretched leg length	0.17	m
k, spring constant	4500	Nm
c, damping constant	42.5	$\frac{Ns}{m}$

5.2 Model Analysis and Exploration

5.2.1 Contact Model Tuning

Due to the hybrid nature of the system and its ability to settle into higher period gaits, the following methodology was used to evaluate the effectiveness of the friction models. For a given model, a Matlab ODE solver was run for a fixed number of steps starting from a given touchdown (TD) velocity (magnitude and angle) on the first leg. The model was initially run for a large number of steps, in this case 1000, to allow the system to settle to a quasi-periodic gait. The TD velocity, as well as the associated clock time, was then recorded for the last successful TD of the first leg. These quasi-periodic parameters were then fed back into the model and it was allowed to run for an additional 100 steps over which the velocity at every TD was recorded as well as initial foot TD locations.

As seen for CT-SLIP in Figure 5.6(a), the magnitude of the velocity was plotted against the angle of the velocity across the TD events. From this data, a limit cycle can be observed of the quasi-periodic gait of CT-SLIP. In addition, the corresponding foot's stride length was plotted against the stride number, where stride length is defined as $stride = p_{1,t} - p_{1,t-1}$ as seen in Figure 5.6(b). The periodic oscillation

about a set value of $0.26m$ is indicative of a higher period, quasi-periodic solution. The common simulation parameters used for all models can be seen in Table 5.1.

The Relative Force Friction (RFF) model was evaluated following the same methodology as CT-SLIP with the exception of the parameter α_{RFF} being varied. For increasing values of α_{RFF}, the TD velocity limit cycle begins to converge onto a fixed point, as seen in Figure 5.7(a). Likewise, Figure 5.7(b) shows the periodic oscillations of the stride length decreasing, while there frequency appears to be increasing. As α increases, it approaches a critical range where the limit cycle converges to a fixed point as seen in Figure 5.8(a). When this happens, the stride length becomes fixed as seen in Figure 5.8(b). However, as α_{RFF} is increased past the critical range, the limit cycle begins to diverge and the stride length becomes irregular. For the RFF model and this model parameter set, the ideal range for quasi-periodic motion seems to be $0.6 \leq \alpha_{RFF} \leq 0.75$.

5.2.2 Model Disturbance Analysis

Once periodic parameters for the friction model had been determined ($\alpha_{\mathrm{RFF}} = 0.75$), the TD velocities for the systems were disturbed by a fixed value and the resulting CoM motion recorded. For both CT-SLIP and the RFF models, the TD velocity was increase by 1m/s from their quasi-periodic steady state TD values. The resulting CoM motion and stride length plots can be seen in Figure 5.9. The disturbed motion (red, solid line) is plotted along with the undisturbed motion (black, hashed line) for return comparison.

The RFF model showed improved settling time from the CT-SLIP model ($\mu = 6.5$). The RFF model returned to its steady state value the quickest as seen in Figure 5.9(a), returning after only 7 strides. However, after 18 strides, the stride length begins to diverge from the steady state as seen in Figure 5.9(b). This becomes apparent if Figure 9a is shown for a larger range of Y positions. The CT-SLIP model returns to its quasi-periodic steady state motion 12 strides after experiencing

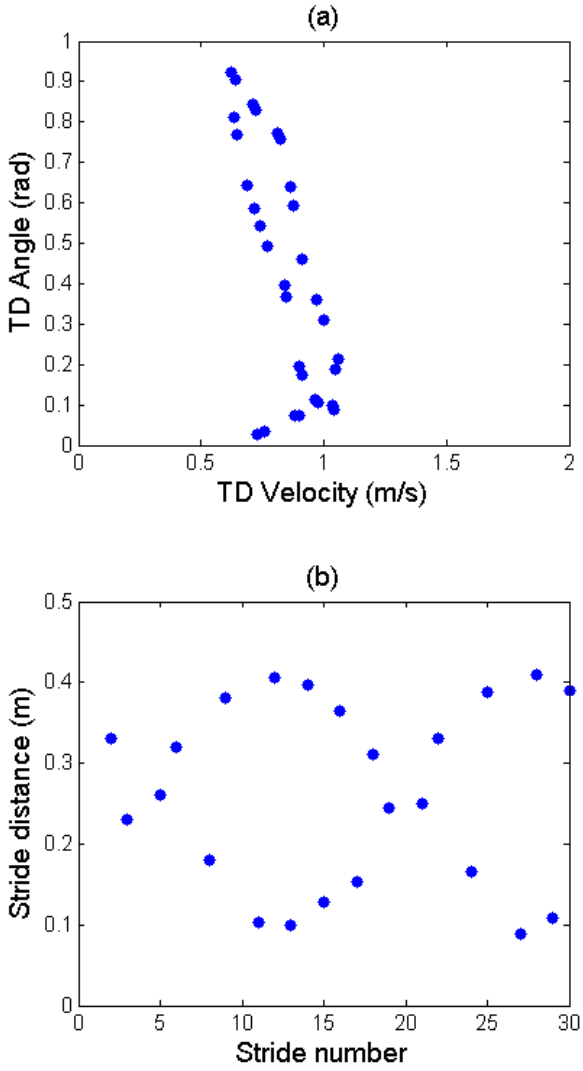

Figure 5.6. No foot slipping, standard CT-SLIP model with the foot contact point modeled as a pin joint. (a) The touchdown (TD) velocity and angle begin to form into a cycle for the fix contact model corresponding to a repeated higher period gait. While quasi-periodic, the TD conditions do not settle to a fixed point with time. (b) The stride length map visually identifies the higher period gait seen in (a).

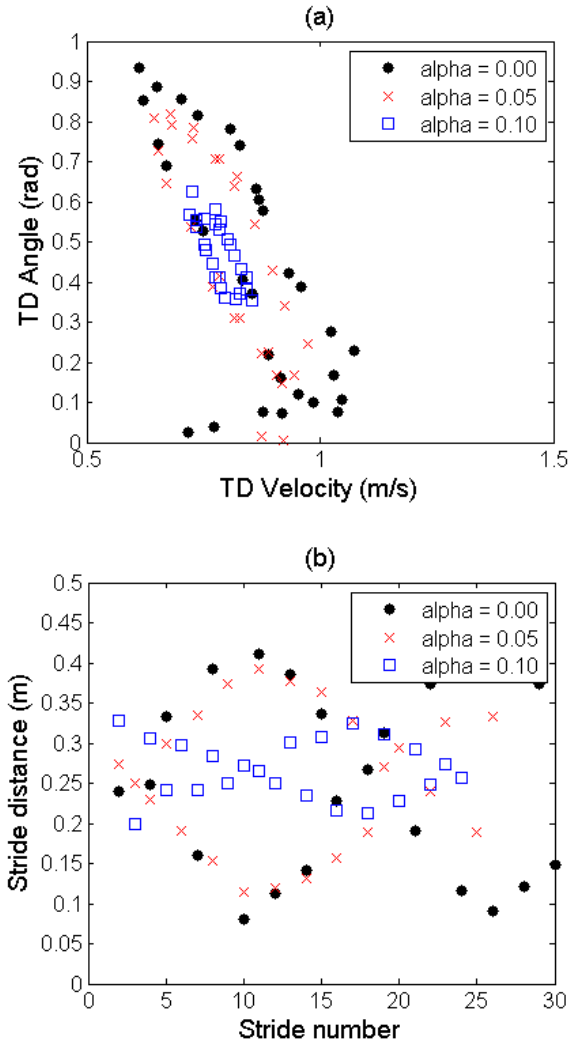

Figure 5.7. Relative Force Friction Model: (a) As α_{RFF} increases from 0 (no foot slipping), the limit cycle of the model decreases. (b) As α_{RFF} increases, the stride length variation decreases and the distance begins to converge on a set value (stride length = $0.26m$).

the disturbance. However, the solution the CoM settles on is 180 degrees out of phase with its original solution. It should be noted, that both models demonstrated this out of phase behavior for some given value of disturbances, either to the TD

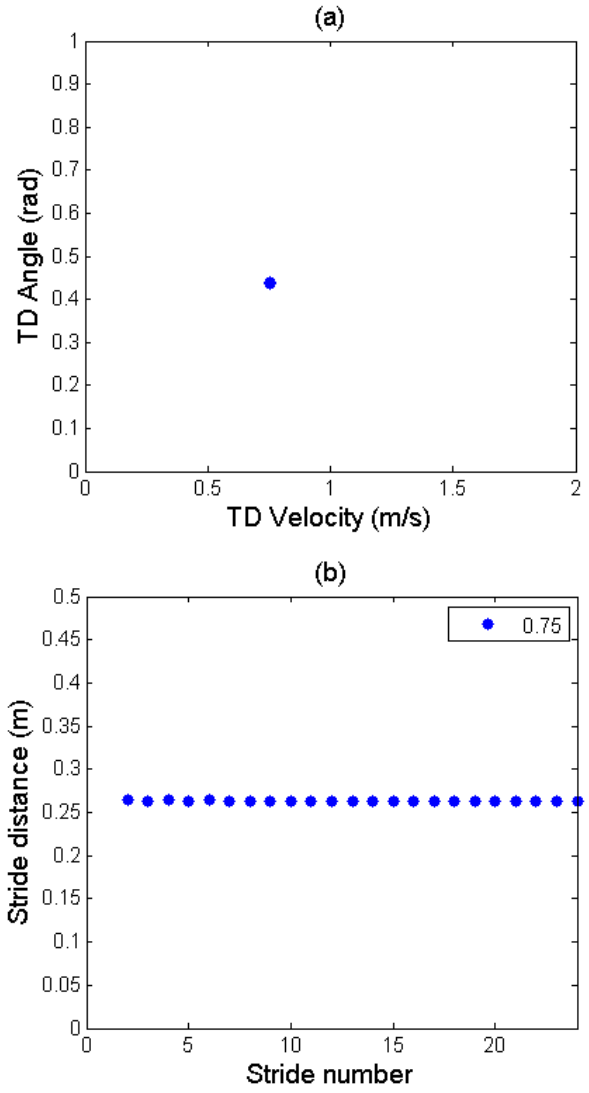

Figure 5.8. Relative Force Friction Model, with $\alpha_{RFF} = 0.75$. (a) As α_{RFF} approaches 0.75, the limit cycle converges to a fixed point indicative of a 1^{st} order periodic gait. (b) As α_{RFF} increases to 0.75, the stride length variation decreases and settles on a fixed value (stride length $= 0.26m$).

velocity magnitude, angle, or both. The frictional model required a significantly larger disturbance to become out of phase when compared to CT-SLIP.

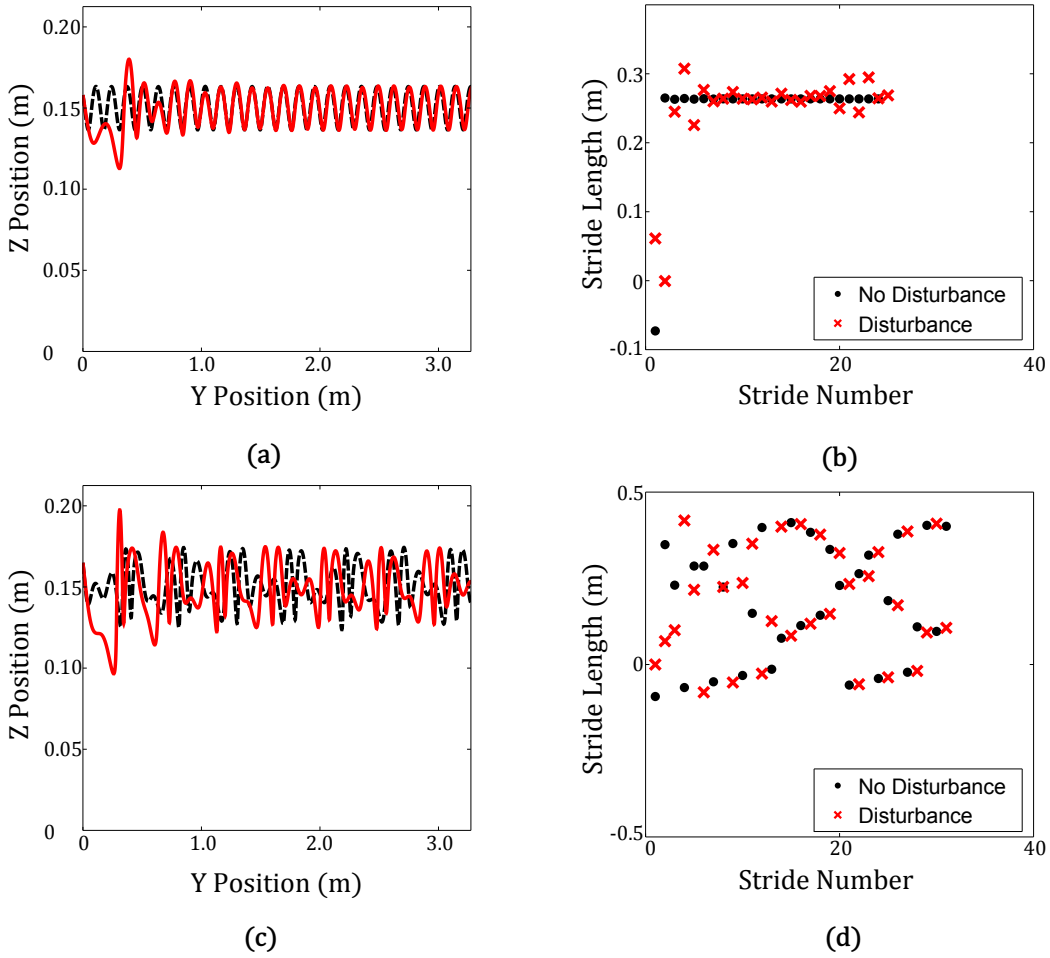

Figure 5.9. Recovery from a fixed velocity perturbation disturbance of 1 m/s for the Relative Force Contact Friction Model (a-b) and CT-SLIP (c-d). The unperturbed steady state model (black, hashed line) is shown alongside the perturbed result (red, solid line) for comparison.

5.3 Experimentally Verifying Frictional Effects

The addition of the RFF friction model to CT-SLIP showed early promise in improving the models qualitative and quantitative motion when compared to experimental data. These initial results encouraged the pursuit of a further experimental study of the effect of changing contact friction parameters on bipedal legged locomotion platforms.

A legged locomotion experiment was developed to test the effect of changing contact friction conditions on the CoM motion. A commercially available hexapod robot (Smart Labs, Bellevue, WA) was utilized as the test platform. The platform has 6 compliant 'S' shaped legs that are driven by a single eletric motor and transmission, locking all of the legs relative to each other. The primary gait of the platform is an alternating tripod, providing a near constant torque while in stance and a constant rotational speed in flight. The base platform can be seen in Figure 5.10.

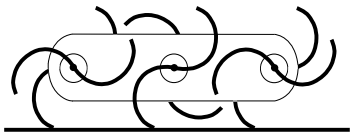

Figure 5.10. Hexapod legged locomotion platform used in experiment.

5.3.1 Design

The experimental test platform was designed to evaluate the center of mass motion of bipedal legged locomotion with changing foot contact friction parameters. The primary design requirements were as follows:

1. Bipedal locomotion constrained to sagittal (XY) plane movement in Figure 5.11,
2. Ability to discretely change foot contact interactions,
3. Reproducible and repeatable starting trial conditions.

The test platform was attached to a pivoting boom mechanism to fix the platform motion to the sagittal plane, as seen in Figure 5.11. The boom can rotate about an anchored central pivot point, allowing forward motion for the test platform while constraining side motion. The platform transcribes an arc defined by the length of the boom, l, and the rotational angle, θ. Additionally, the boom can rotate in the vertical plane about its attachment point, allowing vertical motion in the platform.

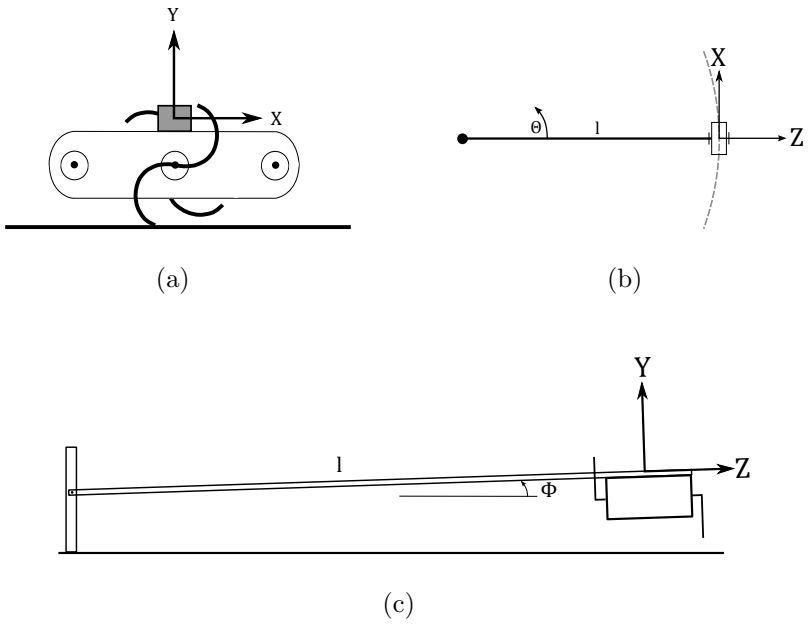

Figure 5.11. Design of experimental locomotion platform used to test foot contact: (a) side view, (b) top view, and (c) front view. The XYZ - coordinate system is moving system fixed to the test platform.

The vertical motion of the platform also transcribes an arc described by the length of the boom, l, and the rotational angle, ϕ. Both pivot points are attached through the use of ball-bearings to reduce frictional losses in the setup. The setup can be seen in Figure 5.12.

The frictional contact dynamics were changed on this platform by exchanging out difference surface materials for the test platform to walk on. In total, three separate materials were used and there descriptions can be found in Table 5.2. Surface materials were secured to the work surface using clamps during testing to prevent material slippage.

5.3.2 Methods

Motion of the test platform was tracked using a Vicon (Boulder, CO) Motion Capture System (4x T160 IR Cameras, 400Hz). Reflective tracking markers were

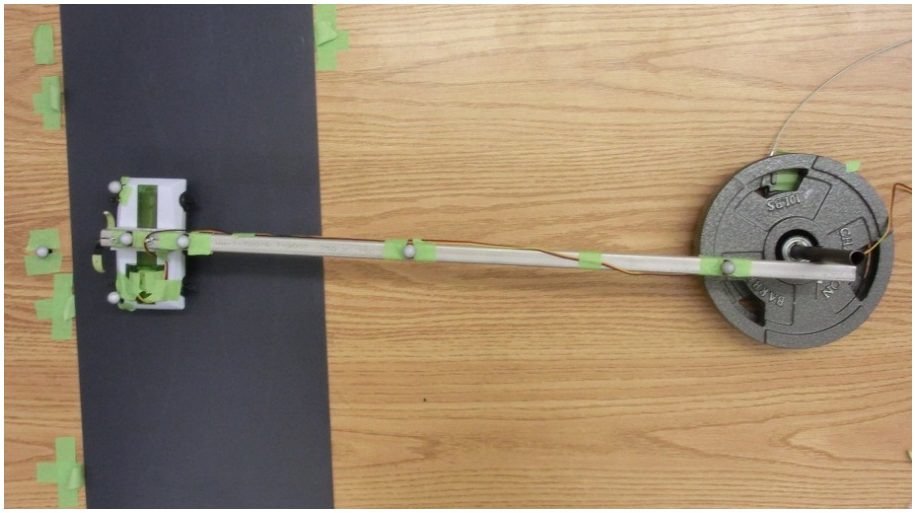

(a)

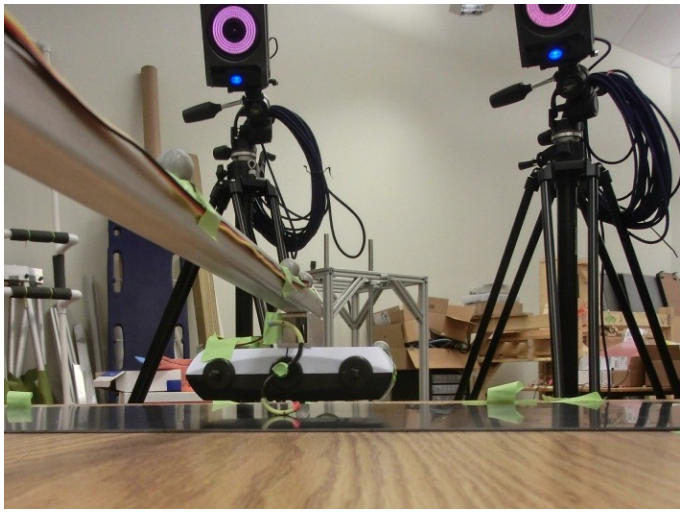

(b)

Figure 5.12. Experimental locomotion platform used to test foot contact: (a) platform view and (b) testing view.

attached to two locations on the boom and the front and back of the test platform to assist in local coordinate system transformations.

For each test material, a designated start location was marked on the surface for each leg. The test platform would begin with the outside leg at touchdown and

Table 5.2.
Frictional contact surface materials exchanged out to evaluate friction effects on locomotion.

Reference #	**Color**	**Grip**	**Material**
13	Gray	Medium	Type 1 PVC
14	Black	Low	ABS
15	White	High	UHMW Polyethyne

the inside leg just toeing off. Care was taken to ensure initial conditions remained constant. A trial capture would begin with the test platform at rest and conclude after an arc length of approximately 0.5 m had been transcribed. Once complete, the leg angles were reset and the test platform placed in the starting location. 10 trials were captured for each material in Table 5.2.

Upon completion of the trials, the marker data was exported to MATLAB for further analysis. After filtering the data for noise (6th order Butterworth, 'low-pass', $f_c = 20Hz$), the marker data was transformed to a rotating coordinate system located on the test platform and described by the angles θ and ϕ, as seen in Figure 5.11. Once the marker movement had been transformed into this direction, the first derivative was taken using the Euler method.

Using the local coordinate system, the forward velocity, v_x, along with a velocity threshold was used to phase correct the experimental data. The mean forward velocity at each time step was then calculated and plotted; they can be seen in Figure 5.13. In addition to the mean forward velocity data, a frequency analysis was also performed for each material. The results can be seen in Figure 5.14.

5.3.3 Results

An analysis of Figure 5.13 reveals that the forward velocities across a single material were fairly consistent during the initial transitions from a stand still to forward

motion. While more data then the $0.75secs$ shown were captured, the trials begin to rapidly diverge after approximately the $0.5secs$ point due to unmodeled dynamics from the test platform. All of the materials share the same initial motion, an approximately linear transition from rest to $500\frac{mm}{s}$ in a time step of $0.2secs$. From that time onward, each of the data sets diverges into its own specific pattern, with different amplitudes and periods. Material#13 shows a large consistent oscillation of $250\frac{mm}{s}$ at a steady period, Material#14 shows a different amplitude peaks with one set at $250\frac{mm}{s}$ and another at $400\frac{mm}{s}$, while Material#15 shows a low amplitude oscillation at $250\frac{mm}{s}$.

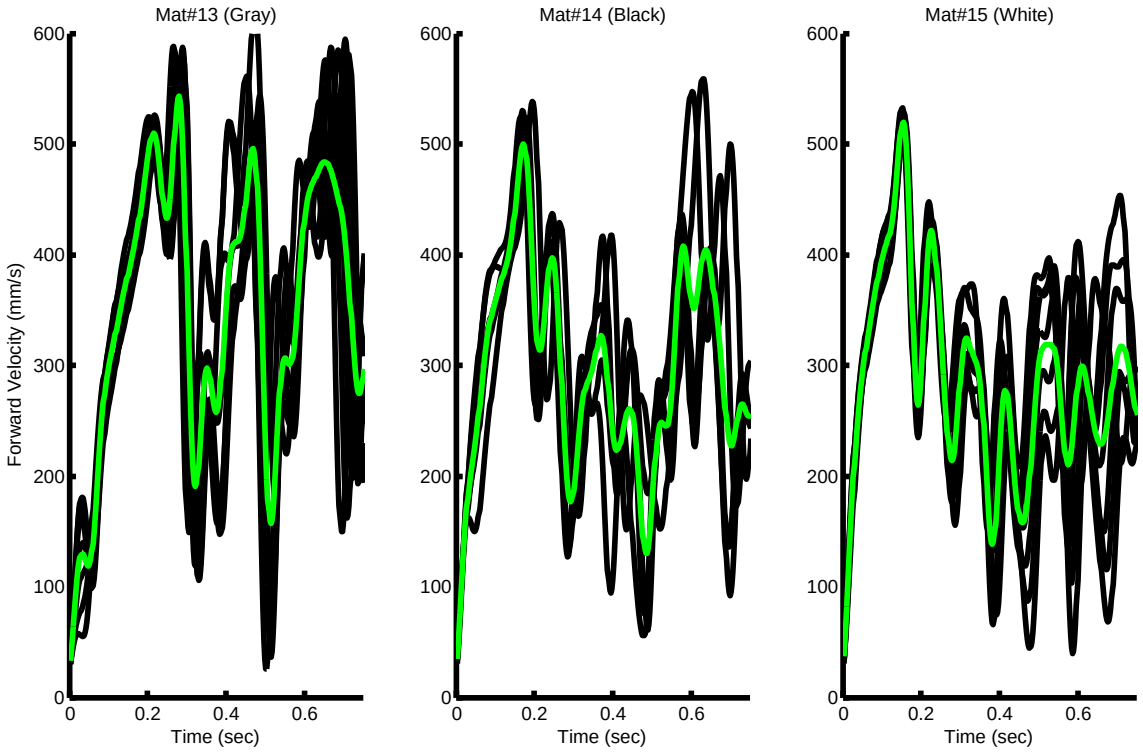

Figure 5.13. Transient Forward Velocity Comparison Across Frictional Values. All 10 trial runs are shown in for each case (black) with the calculated mean overlayed (green).

The presence of higher order periods in the forward velocity of Figure 5.13 influenced an investigation of the frequency content, seen in Figure 5.14. All the material data sets possess components in the same upper frequencies, with significant peaks at 10&15Hz. However, in the lower frequency range, each material has its own signature response. Material#13 & #14, the slicker materials, both have measurable peaks at 5Hz. Additionally, Material#14 has another peak at 2.5Hz. Material#15, the highest grip surface, does not show any notable peaks in the same region.

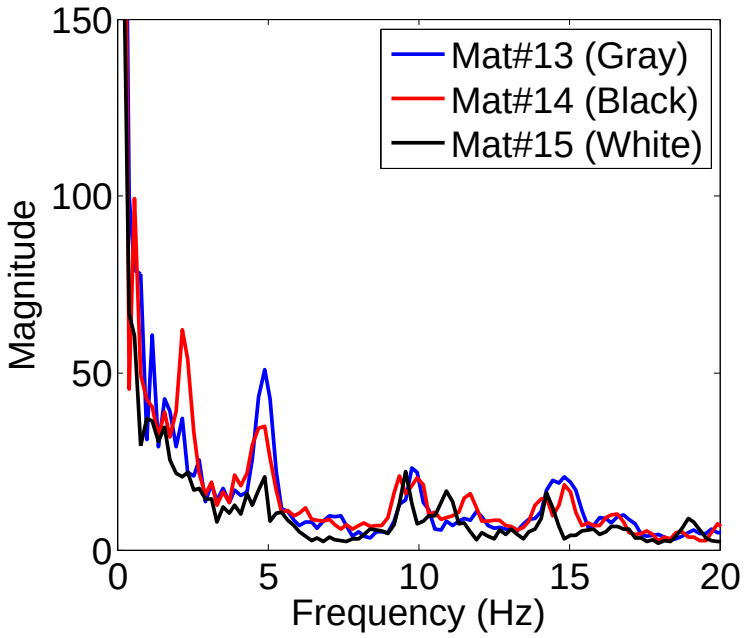

Figure 5.14. FFT analysis of forward velocity across frictional values.

5.4 Discussion

This chapter has developed a model for frictional foot slipping on CT-SLIP. The Relative Friction Force model was tuned to find a critical range for their tuning parameter. Using these tuned parameters, the center of mass motion response to a disturbance was shown and the friction model improved on CT-SLIP's ability to

recover. The ability to withstand higher disturbances was found with the addition of frictional effects. The physical significance of the tuning parameter, α_{RFF}, for the RFF model was not explored in this chapter, though it does warrant further investigation.

An interesting phenomenon was observed in that all of the model's stride lengths converged on or oscillated about a fixed value, $0.26m$. This suggests that the stride length is dependent on other model parameters and not affected by the foot contact model. It is hypothesized that the stride length is primarily a function of the clock parameters and the unstretched leg length. Future work will attempt to explore and evaluate this hypothesis.

An experiment was conducted to measure the effects of friction on bipedal locomotion. The CoM motion of the test platform was recorded over 10 trials on each of three materials with separate surface finishes and nominally different frictional contact interactions. The platform motion was successfully constrained to one a single plane of movement and reproducible transitional forward velocity responses were obtained.

The change in contact surface between the data sets appears to have had an impact on the center of mass kinematics of the test platform. The highest grip material had the slowest average forward velocity of the materials; however, it also experienced the least variation in forward movement speed during the trials. The medium grip material had the highest average forward velocity of the materials but also had the largest variation. The low grip material had the least periodic response with significant variation in average speed. Though it is difficult to be conclusive, there seems to be an optimal target grip for improved forward movement speeds, too high and the overall speed is reduced and too low and the response becomes non-periodic. Likewise, the higher the surface grip, the lower the amplitude of forward speed oscillation; lower gripping surfaces have larger amplitudes of oscillation.

By adding ground contact interactions to CT-SLIP that allow for the feet to slip on the contact surface, a model exhibiting greater resilience to disturbances was

found. Models that include the realistic ability for the contacting point to slip on the surface are better able to mimic the motion of physical systems and warrant further integration into models seeking to improve the quantitative predictive power of locomotion models.

6. CONCLUSIONS

A new technique is presented for mapping and digitally capturing the skin strain on a human subject. This new technique improves upon previous methods [9] by presenting a simplified strain ellipse application process and a method for digitally capturing the location and direction of the LoNE, minimum extension, minimum compression, and negligible deformation nodes along with the complex contours of the leg. This provides an alternative technique to previous studies [3, 10, 11] that allows for direct testing of minimum skin strain contours as a structure for conformal orthotics design.

A notable drawback of this new technique is that it suffers from a large potential for human error while marking the strain circles. If marked incorrectly, there is no provision for correcting the strain directions, leading to noisy or invalid data. Additionally, this technique does not provide a direct method for measuring the skin strain magnitude on the skin surface.

A verification experiment of wraps based on LoNE contours was presented and indicated that the wraps remain conformal to the skin throughout the body's motion, and no significant reduction in the joint's range of motion was observed. Additionally, models of the passive joint behavior of the knee were created and fit to experimental data sets with different orthotic wraps. The linear stiffness of the control data set was validated against an established data set, indicating the joint parameters found through the modeling fit algorithm are reasonable. Significant differences in joint parameters were noted across different data sets, though most significantly between the LoNE based wraps and the Non-LoNE base wrap. This difference indicates that LoNE based structures are at least more optimal than some other possible structures.

A more in-depth study is required to determine the feasibility of using this modeling technique to characterize structures based on LoNE. Chiefly, for a given subject,

the repeatability of joint parameters for a given wrap must be established and the model's ability to predict motion with different initial conditions needs to be explored. Additionally, the resolution and practical limitations of the modeling fit need to be explored before using it to evaluate different configurations of contours across the skin strain vector field.

A locomotion task model exhibiting greater quantitative prediction of center of mass dynamics was found by adding ground contact interactions to an existing legged locomotion model. An experiment was conducted and friction was confirmed to be an important parameter in the center of mass dynamics of a system. Models that include the realistic ability for the contacting point to slip on the surface are better able to mimic the motion of physical systems. Locomotion models seeking to improve their quantitative predictive power should integrate the effects of friction into the model dynamics.

This thesis develops two separate modeling tools for the design of conformal orthotic devices. A tool for modeling the effect of conformal orthotic structures on passive joint parameters is presented, and the initial results are verified. For the exploration of conformal orthotic structure use during human movement tasks, a locomotion model is developed with better quantitative prediction than previously available. Through a better understanding of the interfaces between a user and an orthosis, a paradoxical change in the way orthoses are designed is possible. Through a better understanding of basic human tasks, future systems can be designed to work with their environments to increase user stability and safety. By introducing new tools for the advancement of orthotics, the author hopes to enable a world of technology that improves quality of life by improving human motion.

LIST OF REFERENCES

LIST OF REFERENCES

[1] K. A. Shorter, X. Jicheng, E. T. Hsiao-Wecksler, W. K. Durfee, and G. F. Kogler. Technologies for powered ankle-foot orthotic systems: Possibilities and challenges. *Mechatronics, IEEE/ASME Transactions on*, 18(1):337–347, 2011.

[2] A. M. Dollar and H. Herr. Lower extremity exoskeletons and active orthoses: Challenges and state-of-the-art. *Robotics, IEEE Transactions on*, 24(1):144–158, 2008.

[3] K. Bethke. *The second skin approach: Skin strain field analysis and mechanical counter pressure prototyping for advanced spacesuit design*. PhD thesis, Massachusetts Institute of Technology, 2005.

[4] D. Newman, J. Hoffman, K. Bethke, J. Blaya, C. Carr, and B. Pitts. Astronaut bio-suit system for exploration class missions. *NIAC Phase II Final Report*, 2005.

[5] B. Vanderborght, R. Van Ham, D. Lefeber, T. G. Sugar, and K. W. Hollander. Comparison of mechanical design and energy consumption of adaptable, passive-compliant actuators. *The International Journal of Robotics Research*, 28(1):90–103, 2009.

[6] D. Ferris, G. Sawicki, and M. Daley. A physiologist's perspective on robotic exoskeletons for human locomotion. *Internation Journal of Humanoid Robotics*, 4(3):507–528, 2007.

[7] M. Zinn, O. Khatib, B. Roth, and J. K. Salisbury. Playing it safe [human-friendly robots]. *Robotics & Automation Magazine, IEEE*, 11(2):12–21, 2004.

[8] T. G. Sugar. A novel selective compliant actuator. *Mechatronics*, 12(910):1157–1171, 2002.

[9] A. Iberall. The use of lines of nonextension to improve mobility in full-pressure suits. Technical report, DTIC Document, 1964.

[10] S. Marreiros. *Skin Strain Field Analysis of the Human Ankle Joint*. PhD thesis, Universidade de Lisboa, 2010.

[11] A. Wessendorf and D. Newman. Dynamic understanding of human-skin movement and strain-field analysis. *Biomedical Engineering, IEEE Transactions on*, 59(12):3432–3438, 2012.

[12] R. Wartenberg. Pendulousness of the legs as a diagnostic test. *Neurology*, 1(1):18, 1951.

[13] M. Srinivasan and P. Holmes. How well can spring-mass-like telescoping leg models fit multi-pedal sagittal-plane locomotion data? *Journal of theoretical biology*, 255(1):1–7, 2008.

[14] J. Seipel and P. Holmes. A simple model for clock-actuated legged locomotion. *Regular and Chaotic Dynamics*, 12(5):502–520, 2007.

[15] A. Iberall. The experimental design of a mobile pressure suit. *Journal of Basic Engineering*, 92:251, 1970.

[16] W. Schwind. *Spring loaded inverted pendulum running: a plant model*. PhD thesis, University of Michigan, 1998. Chair - Daniel E. Koditschek.

[17] G. J. Tortora. *Introduction to the human body : the essentials of anatomy and physiology*. Hoboken, NJ : J. Wiley and Sons, Hoboken, NJ, 2004.

[18] R. A. Heinlein. *Starship Troopers*. Putnam, New York, 1959.

[19] D. Winter. *Biomechanics and Motor Control of Human Movement*. John Wiley and Sons, Inc., 4th edition, 2009.

[20] K. W. Hollander, R. Ilg, T. G. Sugar, and D. Herring. An efficient robotic tendon for gait assistance. *Journal of Biomechanical Engineering*, 128(5):788–791, 2006.

[21] E. Garcia, J. M. Sater, and J. Main. Exoskeletons for human performance augmentation (ehpa) : A program summary. *Journal of the Robotics Society of Japan*, 20(8):822–826, 2002.

[22] H. Kazerooni and R. Steger. The berkeley lower extremity exoskeleton. *Trans. ASME, J. Dyn. Syst., Meas., Control*, 128:14–25, 2006.

[23] E. Guizzo and H. Goldstein. The rise of the body bots [robotic exoskeletons]. *Spectrum, IEEE*, 42(10):50–56, 2005.

[24] C. J. Walsh, K. Pasch, and H. Herr. An autonomous, underactuated exoskeleton for load-carrying augmentation. In *Intelligent Robots and Systems, 2006 IEEE/RSJ International Conference on*, pages 1410–1415, 2006.

[25] A. Chu, H. Kazerooni, and A. Zoss. On the biomimetic design of the berkeley lower extremity exoskeleton (bleex). In *Robotics and Automation, 2005. ICRA 2005. Proceedings of the 2005 IEEE International Conference on*, pages 4345–4352, 2005.

[26] H. Kelly. Lockheed martin unveils exoskeleton technology at ausa winter symposium.

[27] C. J. Walsh, D. Paluska, K. Pasch, W. Grand, A. Valiente, and H. Herr. Development of a lightweight, underactuated exoskeleton for load-carrying augmentation. In *Robotics and Automation, 2006. ICRA 2006. Proceedings 2006 IEEE International Conference on*, pages 3485–3491, 2006.

[28] C.J. Walsh, K. Endo, and H. Herr. A quasi-passive leg exoskeleton for load-carrying augmentation. *International Journal of Humanoid Robotics*, 4(3):487–506, 2007.

[29] H. Kawamoto and Y. Sankai. Power assist system hal-3 for gait disorder person. *Proc. Int. Conf. Comput. Helping People Special Needs (ICCHP)*, 2398, 2002.

[30] H. Kawamoto, L. Suwoong, S. Kanbe, and Y. Sankai. Power assist method for hal-3 using emg-based feedback controller. In *Systems, Man and Cybernetics, 2003. IEEE International Conference on*, volume 2, pages 1648–1653 vol.2, 2003.

[31] J. A. Blaya and H. Herr. Adaptive control of a variable-impedance ankle-foot orthosis to assist drop-foot gait. *Neural Systems and Rehabilitation Engineering, IEEE Transactions on*, 12(1):24–31, 2004.

[32] D. P. Ferris, K. E. Gordon, G. S. Sawicki, and A. Peethambaran. An improved powered anklefoot orthosis using proportional myoelectric control. *Gait and Posture*, 23(4):425–428, 2006.

[33] J. K. Hitt, T. G. Sugar, M. Holgate, and R. Bellman. An active foot-ankle prosthesis with biomechanical energy regeneration. *Journal of Medical Devices*, 4(1):011003–9, 2010.

[34] F. H. Silver, L. M. Siperko, and G. P. Seehra. Mechanobiology of force transduction in dermal tissue. *Skin Research and Technology*, 9(1):3–23, 2003.

[35] F. M. Hendriks, D. Brokken, C. W. J. Oomens, D. L. Bader, and F. P. T. Baaijens. The relative contributions of different skin layers to the mechanical behavior of human skin in vivo using suction experiments. *Medical Engineering and Physics*, 28(3):259–266, 2006.

[36] C. Escoffier, J. de Rigal, A. Rochefort, R. Vasselet, J. Leveque, and P. G. Agache. Age-related mechanical properties of human skin: An in vivo study. *J Investig Dermatol*, 93(3):353–357, 1989.

[37] G. J. Tortora. *Introduction to the human body: the essentials of anatomy and physiology*. John Wiley and Sons, Inc., 6th edition, 2004.

[38] O. Kuwazuru, J. Saothong, and N. Yoshikawa. Mechanical approach to aging and wrinkling of human facial skin based on the multistage buckling theory. *Medical Engineering and Physics*, 30(4):516–522, 2008.

[39] A. B. Cua, K. P. Wilhelm, and H. I. Maibach. Elastic properties of human skin: relation to age, sex, and anatomical region. *Archives of Dermatological Research*, 282(5):283–288, 1990.

[40] Z. Liu and K. Yeung. The preconditioning and stress relaxation of skin tissue. *J Biomech Eng*, 2(1):22–28, 2008.

[41] A. Vexler, I. Polyansky, and R. Gorodetsky. Evaluation of skin viscoelasticity and anisotropy by measurement of speed of shear wave propagation with viscoelasticity skin analyzer1. *Journal of Investigative Dermatology*, 113(5):732–739, 1999.

[42] C. Pailler-Mattei, S. Bec, and H. Zahouani. In vivo measurements of the elastic mechanical properties of human skin by indentation tests. *Medical Engineering and Physics*, 30(5):599–606, 2008.

[43] B. Holt, A. Tripathi, and J. Morgan. Viscoelastic response of human skin to low magnitude physiologically relevant shear. *Journal of Biomechanics*, 41(12):2689–2695, 2008.

[44] J. E. Sanders, B. S. Goldstein, and D. F. Leotta. Skin response to mechanical stress: Adaptation rather than breakdown–a review of the literature. *Journal of Rehabilitation Research and Development*, 32(3):214–26, 1995. Copyright - Copyright Superintendent of Documents Oct 1995 Last updated - 2012-04-11 CODEN - JRRDDB DOI - 8696613; 463683; 20977; JRRDDB; PJHB; 8592293; 02602058; 95416286.

[45] K. Langer. On the anatomy and physiology of the skin: I. the cleavability of the cutis. *British journal of plastic surgery*, 31(1):3–8, 1978.

[46] P. Elsner. *Bioengineering of the skin : skin biomechanics*. Boca Raton : CRC Press, Boca Raton, 2002. Includes bibliographical references and index.

[47] R. F. Edlich and B. A. Carl. Predicting scar formation: from ritual practice (langer's lines) to scientific discipline (static and dynamic skin tensions).

[48] T. Bajd and B. Bowman. Testing and modelling of spasticity. *Journal of Biomedical Engineering*, 4(2):90–96, 1982.

[49] M. Valle, A. Casabona, R. Sgarlata, R. Garozzo, M. Vinci, and M. Cioni. The pendulum test as a tool to evaluate passive knee stiffness and viscosity of patients with rheumatoid arthritis. *BMC Musculoskeletal Disorders*, 7(1):89, 2006.

[50] T. Bajd and L. Vodovnik. Pendulum testing of spasticity. *Journal of Biomedical Engineering*, 6(1):9–16, 1984.

[51] M. Jamshidi and A. W. Smith. Clinical measurement of spasticity using the pendulum test: Comparison of electrogoniometric and videotape analyses. *Archives of Physical Medicine and Rehabilitation*, 77(11):1129–1132, 1996.

[52] R. Full and D. Koditschek. Templates and anchors: neuromechanical hypotheses of legged locomotion on land. *Journal of Experimental Biology*, 202(23):3325–3332, 1999.

[53] Z. H. Shen and J. E. Seipel. A fundamental mechanism of legged locomotion with hip torque and leg damping. *Bioinspiration & Biomimetics*, 7(4):046010, 2012.

[54] R. J. Full and M. S. Tu. Mechanics of a rapid running insect: Two-, four-, and six-legged locomotion. *J Exp. Biology*, 156:215–231, 1991.

[55] K. Autumn J. I. Chung R.J. Full and A. Ahn. Rapid negotiation of rough terrain by the death-head cockroach. *American zoologist*, 38, 1998.

[56] U. Saranli, M. Buehler, and D. Koditschek. Rhex: A simple and highly mobile hexapod robot. *The International Journal of Robotics Research*, 20(7):616–631, 2001.

[57] N. Neville, M. Buehler, and I. Sharf. A bipedal running robot with one actuator per leg. In *Robotics and Automation, 2006. ICRA 2006. Proceedings 2006 IEEE International Conference on*, pages 848–853, 2006.

[58] D. McMordie and M. Buehler. Towards pronking with a hexapod robot. *Int. Conf. Climbing and Walking Robots*, pages 659–666, 2001.

[59] E. Z. Moore, D. Campbell, F. Grimminger, and M. Buehler. Reliable stair climbing in the simple hexapod 'rhex'. In *Robotics and Automation, 2002. Proceedings. ICRA '02. IEEE International Conference on*, volume 3, pages 2222–2227, 2002.

[60] U. Saranli and D. E. Koditschek. Back flips with a hexapedal robot. In *Robotics and Automation, 2002. Proceedings. ICRA '02. IEEE International Conference on*, volume 3, pages 2209–2215, 2002.

[61] D. Campbell and M. Buehler. Preliminary bounding experiments in a dynamic hexapod. *Lecture Notes in Control and Information Sciences*, pages 612–621, 2003.

[62] J. Rummel and A. Seyfarth. Stable running with segmented legs. *The International Journal of Robotics Research*, 27(8):919–934, 2008.

[63] M. H. Tello and E. R. Raibert. Legged robots that balance. *IEEE Expert*, 1:89–89, 1986.

[64] S. Riddle, A. Cherian, and J. Seipel. Mapping the skin strain vector field of the human body. In *IDETC/CIE 2013*. ASME, 2013.

[65] J. Waldie and D. Newman. A gravity loading countermeasure skinsuit. *Acta Astronautica*, 68(78):722–730, 2011.

[66] K. P. Granata, S. E. Wilson, and D. A. Padua. Gender differences in active musculoskeletal stiffness. part i.: Quantification in controlled measurements of knee joint dynamics. *Journal of Electromyography and Kinesiology*, 12(2):119–126, 2002.

[67] K. P. Granata, D. A. Padua, and S. E. Wilson. Gender differences in active musculoskeletal stiffness. part ii. quantification of leg stiffness during functional hopping tasks. *Journal of Electromyography and Kinesiology*, 12(2):127–135, 2002.

[68] S. P. Magnusson. Passive properties of human skeletal muscle during stretch maneuvers. *Scandinavian Journal of Medicine & Science in Sports*, 8(2):65–77, 1998.

[69] R. Altendorfer, N. Moore, H. Komsuoglu, M. Buehler, Jr. Brown, H. B., D. McMordie, U. Saranli, R. Full, and D. E. Koditschek. Rhex: A biologically inspired hexapod runner. *Autonomous Robots*, 11(3):207–213, 2001.

[70] M. A. Sherman, A. Seth, and S. L. Delp. Simbody: multibody dynamics for biomedical research. *Procedia IUTAM*, 2(0):241–261, 2011.

[71] S. L. Delp, F. C. Anderson, A. S. Arnold, P. Loan, A. Habib, C. T. John, E. Guendelman, and D. G. Thelen. Opensim: Open-source software to create and analyze dynamic simulations of movement. *Biomedical Engineering, IEEE Transactions on*, 54(11):1940–1950, 2007.